

The dynamics of an insulating plate over a thermally convecting fluid and its implication for continent movement over convective mantle

Yadan Mao^{1,†}, Jin-Qiang Zhong² and Jun Zhang^{3,4}

¹Hubei Subsurface Multi-scale Imaging Key Laboratory, Institute of Geophysics and Geomatics, China University of Geosciences, Wuhan 430074, China

²School of Physics Science and Engineering, Tongji University, Shanghai 200092, China

³Courant Institute, and Department of Physics, New York University, New York, NY 10012, USA

⁴NYU-ECNU Institute of Physics, NYU Shanghai, Shanghai 200062, China

(Received 20 May 2018; revised 28 February 2019; accepted 28 February 2019;
first published online 11 April 2019)

Continents exert a thermal blanket effect to the mantle underneath by locally accumulating heat and modifying the flow structures, which in turn affects continent motion. This dynamic feedback is studied numerically with a simplified model of an insulating plate over a thermally convecting fluid with infinite Prandtl number at Rayleigh numbers of the order of 10^6 . Several plate–fluid coupling modes are revealed as the plate size varies. In particular, small plates show long durations of stagnancy over cold downwellings. Between long stagnancies, bursts of velocity are observed when the plate rides on a single convection cell. As plate size increases, the coupled system transitions to another type of short-lived stagnancy, in which case hot plumes develop underneath. For an even larger plate, a unidirectional moving mode emerges as the plate modifies impeding flow structures it encounters while maintaining a single convection cell underneath. These identified modes are reminiscent of some real cases of continent–mantle coupling. Results show that the capability of a plate to overcome impeding flow structures increases with plate size, Rayleigh number and intensity of internal heating. Compared to cases with a fixed plate, cases with a freely drifting plate are associated with higher Nusselt number and more convection cells within the flow domain.

Key words: convection in cavities, mantle convection

1. Introduction

Being ubiquitous in nature, thermal convection presents itself in many natural flows. Warm air rising above solar-heated land or water generates convective cells that contribute to all weather systems. Large-scale oceanic circulation is also generated by thermal convection, as cold surface water at high latitudes sinks deep and flows towards the equator and warm equator water floats towards higher latitudes, resulting in an overturning circulation. These natural convection events occur in fluid. Given enough time, thermal convection can even occur in Earth's solid mantle by means of solid-state creep (Turcotte & Schubert 2002). In fact, the realization that the

† Email address for correspondence: yadan_mao@cug.edu.cn

mantle can exhibit viscous behaviour on a geologic time scale is crucial in conjuring up mantle convection as the driving force for continental drift, which leads to the birth of the revolutionary theory of plate tectonics (Schubert, Turcotte & Olson 2001).

Compared to the oceanic lithosphere, the average heat loss through continents is much lower (Pollack, Hurter & Johnson 1993; Lenardic *et al.* 2005). The presence of continents limits local surface heat flux and warms up the underlying mantle, thus modifying the underlying flow structure, which in turn affects continent motion. Therefore, continents and the mantle form a strongly coupled dynamic system. This is analogous to a simplified model of an insulating plate drifting over a thermally convecting fluid, which has been adopted in laboratory experiments (Elder 1967; Zhang & Libchaber 2000; Zhong & Zhang 2005; Whitehead, Shea & Behn 2011). The process was also modelled experimentally by a freely moving heat source over a thermally convecting fluid (Howard, Malkus & Whitehead 1970; Whitehead 1972). Simplified though they are, these models capture the essential factors and the basic mechanisms, in particular, (1) a thermally convecting fluid subject to basal heating; (2) a plate drifting on top of the fluid; (3) the dynamic feedback between the plate and the convecting fluid.

In the present study, the emphasis is placed on the dynamic feedback between a freely drifting plate and the thermally convecting fluid underneath it. How does a freely drifting plate affect underlying convection and what dynamic states can it trigger? Replacing the freely drifting plate with a rigid wall sealing the top of the fluid results in the classic problem of Rayleigh–Bénard convection, for which one of the key issues is the overall efficiency of heat transport through the fluid (Ahlers, Grossmann & Lohse 2009). For the present coupled system, we will investigate how a freely drifting plate affects the overall heat transport efficiency of the fluid as compared to the case with a fixed plate.

Rather than being a passive drifter, a floating plate moves without requiring a pre-existing stream in the fluid, as discovered very early through laboratory experiments (Elder 1967). More recently, laboratory experiments show that a floating plate over a convecting fluid oscillates periodically between the two end walls of the fluid domain (Zhang & Libchaber 2000; Zhong & Zhang 2005). This suggests that low-dimensional behaviour can be restored in turbulent Bénard convection by introducing a freely moving boundary. As the plate covers an increasing portion of the top surface, a trapped state starts to appear in which the floating plate stays in the middle of the flow domain and makes only small excursions in response to the competition between the two underlying convection cells (Zhong & Zhang 2007*a,b*). Nevertheless, the fluid in these experiments is water, the Prandtl number of which is far from that of the mantle. Furthermore, the aspect ratios of the fluid domain in these experiments are much smaller than that of the Earth. These differences bring uncertainty when applying the experimental results to the Earth itself.

Meanwhile, numerical methods utilizing dynamically determined boundary conditions have captured processes of continent aggregation and dispersion and the simultaneous development of underlying mantle flow (Gurnis 1988; Lowman & Jarvis 1993, 1995; Lowman & Gable 1999; Honda *et al.* 2000; Heron & Lowman 2011). Moreover, important light has been shed on the long-term dynamic feedback between the plate and the underlying flow (Gurnis 1988; Zhong & Gurnis 1993; Phillips & Bunge 2005; Whitehead & Behn 2015). An interesting feature is that time series of plate velocity had suggested that a plate's motion varies with its size: very large plates always have an appreciable velocity, whereas the velocity of small plate is episodic, with low velocities interrupted by bursts of high velocities (Gurnis 1988; Phillips & Bunge 2005). But the details of this variation and the mechanism underlying this variation are unclear. More recently, a 'continental drift convection cell' has been observed in

the numerical study of Whitehead & Behn (2015), in which a single convection cell is always identified underlying the drifting plate, moving with the plate and absorbing ambient cells on its way. However, the presence of the single cell and the periodic motion of the plate are only steady for relatively large plates. What happens when plates are small? It is expected that small plates are less capable of modulating the underlying mantle flow and should behave more passively. Therefore, plate motion and the evolution of underlying flow are expected to vary with plate size. But how exactly plate motion and the associated underlying flow depend on plate size is still unclear.

To answer this question, we numerically simulate the coupled dynamic system with a mobile plate of a wide range of sizes over a thermally convecting fluid with infinite Prandtl number. Our results shed light on the above question and reveal three different coupling modes: namely, the stagnant mode I (SM I), stagnant mode II (SM II) and the unidirectionally moving mode (UMM) as plate size increases. These different modes might illustrate, to a certain extent, the variation of continent–mantle coupling over the convective mantle, as discussed in §5.

The remainder of the paper is organized as follows: First, the numerical model and techniques are given in §2. The evolutions of three distinct coupling modes are then demonstrated in detail for the two-dimensional (2-D) cases in §3 and briefly for the three-dimensional (3-D) cases later in §4.6. Section 4 presents detailed analysis on the simulation results. In this section, the variation of plate speed with plate size is analysed, and a comparison of Nusselt number is made between cases with a freely moving plate and those with a fixed plate. The variation of plate motion with Rayleigh number, the effect of internal heating on plate motion, and the evolution of different modes in three dimensions are also investigated in this section. Finally, a brief summary and the relation of the identified coupling modes to real geophysical phenomena are given in §5.

2. Numerical simulations

Most of the simulations in the present study are performed for the 2-D models, but some 3-D simulation results are presented in §4.6. Our numerical model incorporates several simplifications, as in previous studies (for example, Gurnis 1988; Whitehead & Behn 2015): a 2-D or a 3-D rectangular geometry, the Boussinesq approximation, a uniform viscosity for the convecting fluid, and the dropping of the inertia and advection terms in the momentum equation owing to the large Prandtl number of the mantle. Here, we focus on revealing the different coupling modes caused by the ‘thermal blanket effect’, which may be obscured when complex Earth-like factors are considered. Therefore, the ‘thermal blanket effect’ of continents is studied in isolation and the simulation is conducted in a much reduced system with only the essential factors. A Cartesian coordinate system is considered, with coordinate components x_i ($i = 1, 2$ for the 2-D system; $i = 1, 2, 3$ for the 3-D system), where x_2 represents the vertical coordinate. The velocity components are denoted as u_i , and the symbols t , P , T , and h represent time, pressure, temperature and internal heating rate, respectively. With the above assumptions, the dimensionless governing equations become:

$$\frac{\partial u_i}{\partial x_i} = 0 \quad (2.1)$$

$$\frac{\partial^2 u_i}{\partial x_j \partial x_j} = Ra \frac{\partial P}{\partial x_i} - Ra \delta_{i2} T \quad (2.2)$$

$$\frac{\partial T}{\partial t} + u_j \frac{\partial T}{\partial x_j} = \frac{\partial^2 T}{\partial x_j \partial x_j} + h, \quad (2.3)$$

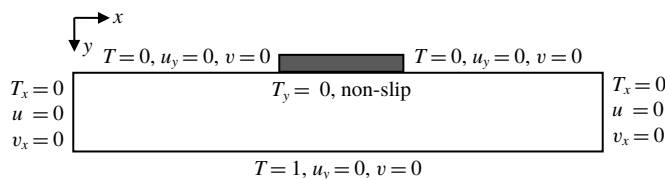


FIGURE 1. Sketch of the model and specification of boundary conditions for the 2-D cases.

where the symbol δ_{ij} denotes the Kronecker delta ($\delta_{ij} = 1$ if $i = j$, $\delta_{ij} = 0$ if $i \neq j$). The Rayleigh number Ra is defined as $Ra = g\beta\Delta TD^3/(\nu\kappa)$, where g , ΔT , D , β , ν and κ are the acceleration due to gravity, temperature difference between the bottom and the top of the fluid, the depth of the fluid domain, thermal expansion coefficient, kinematic viscosity, and thermal diffusivity of the fluid, respectively. The flow can be turbulent even for infinite Prandtl number, owing to the nonlinearity in the energy equation (2.3). The average Nusselt number Nu over the bottom surface is defined as

$$Nu = \frac{q}{k \frac{\Delta T}{D}}, \tag{2.4}$$

where k is the thermal conductivity and q is the average heat flux at the bottom of the flow domain. Equations (2.1)–(2.3) are made dimensionless with the following scales: the coordinate x_i scale D , the time t scale D^2/κ , the temperature T (relative to the top surface temperature) scale ΔT , the velocity u_i scale κ/D , the pressure gradient $\partial P/\partial x_i$ scale $\rho_0 g \beta \Delta T$ (ρ_0 is the fluid density), the internal heating rate h scale $\rho_0 c_p \kappa \Delta T/D^2$ (c_p is the specific heat). For simplicity, the indicial notation is substituted hereinafter by the basic Cartesian notation, where $x = x_1$, $y = x_2$, $z = x_3$. Correspondingly, the velocity components u_1, u_2, u_3 are denoted as u, v, w , respectively. The vertical normal stress σ_{yy} , discussed later, is normalized by $\rho_0 \nu \kappa/D^2$.

The fluid is initially stationary and isothermal ($T = 1$). The vertical end walls are set to be adiabatic. The bottom of the chamber is set to be isothermal ($T = 1$). Cooling ($T = 0$) is imposed on top of the fluid. The limited heat flux through the continent is simplified by setting it to zero at the plate–fluid interface, i.e. the plate bottom, as also adopted by Whitehead & Behn (2015). All the boundaries of the fluid are set to be stress-free except the plate–fluid interface, which is set to be non-slip, i.e. flow at the interface has the same velocity as the plate. A schematic figure of the 2-D model is shown in figure 1 with the boundary conditions denoted, where variables with a subscript denote the partial derivatives with respect to the subscript (for example, $u_y = \partial u/\partial y$). For the 2-D models, a 2-D convection domain with an aspect ratio of 8 ($W/D = 8$, where W and D are the horizontal span and the depth of the fluid domain, respectively) is considered (figure 1). The plate length L , normalized by D , varies from 0.25 to 5.

For fluid with infinite Prandtl number, body forces are balanced by viscous forces, and thus there is no acceleration or net force on any mass element (Gable, O’Connell & Travis 1991). The plate has no inertia. Therefore, the plate velocity is determined by setting the net horizontal shear force exerted by the flow on the plate–fluid interface (plate bottom) to zero. Plate velocity determined this way was first used by Gable *et al.* (1991). It ensures energy conservation, neither adding nor subtracting energy from the convecting system (Lowman & Jarvis 1999). Therefore, plate velocity

is specified by the integral of flow velocity at the first grid cell below the interface. Both the flow velocity and the plate position are updated at each time step. When the plate encounters the end walls, its speed is set to be zero until the net underlying flow reverses. The governing equations along with the specified boundary and initial conditions are solved numerically using the finite-volume method. The code has been used and validated when solving natural convection problems (for example, Mao, Lei & Patterson 2009, 2010). The SIMPLE scheme (Patankar 1980) is adopted for pressure–velocity coupling and the QUICK scheme (Leonard 1979) is applied for spatial derivatives. A second-order implicit scheme is applied for time discretization.

For each run of the 2-D cases, the plate is first fixed in the middle at the top of the fluid ($y = 0$) until a quasi-steady-state is reached, and then the plate is set free. A mesh and time-step dependency test has been conducted for three different meshes, 400×50 , 800×100 , 1200×150 , for the fixed plate case in the 2-D system with a plate length of $L = 0.25$ and $Ra = 10^6$ (Appendix). All the meshes were equidistant and the time step is adjusted so that the Courant–Friedrichs–Lewy (CFL) number remains the same for different meshes. The averaged Nusselt number Nu at quasi-steady-state (averaged from $t = 0.3$ to 0.5) for the three different meshes (from the coarsest to the finest) is 13.88, 16.66, 17.25. The difference of Nu decreases from 20.0% between the former two meshes to 3.5% between the latter two. In order to ensure the accuracy of the solutions while keeping the calculation time manageable, the 800×100 mesh is used in all the following 2-D simulations with a time step of 5×10^{-7} .

For the 3-D coordinate system, the axes of x and z lie within the horizontal domain, and the y axis is also in the direction of the depth as in the 2-D system. A mesh of $400 \times 400 \times 50$ was adopted for a $8 \times 8 \times 1$ fluid domain (8×8 is the horizontal dimension and 1 is the depth). Similar to the 2-D cases, there is no net force on the plate exerted by the fluid to ensure energy conservation of the convecting system. As a result, the translational movement of the plate in the x – z plane ensures that there is no net force in the directions of the two horizontal axes, x and z . Therefore, both the integral of shear stress τ_{xy} (proportional to $\partial(u - u_c)/\partial y$, where u is the x -component of fluid speed adjacent the interface and u_c is the x -component of the net plate speed) and the integral of τ_{zy} (proportional to $\partial(w - w_c)/\partial y$, where w is the z -component of fluid speed adjacent the interface and w_c is the z -component of the net plate speed) on the interface (plate bottom) are zero. The rotational movement of the plate in the horizontal plane ensures no net shear force τ_{xz} (proportional to $2^{-1}(\partial u/\partial z - \partial w/\partial x) - \omega_c$, where ω_c is the angular speed of the plate, the rotational axis is parallel to the y axis at plate centre) is exerted by the flow on plate bottom. These conditions uniquely determine the movement of the plate. Three plate sizes, with horizontal dimensions of 0.5×0.5 , 1.5×1.5 and 2.5×2.5 are adopted to demonstrate the presence of three different modes in three dimensions. The plate is initially placed at the centre of the top surface of the fluid domain. Different from the 2-D case, the plate is set free to move from the beginning when the entire flow is isothermal and stationary. Since 3-D simulation is much more time-consuming than 2-D simulation, a much shorter time series is obtained for the 3-D cases than the 2-D cases.

3. Coupling modes

A plate moves along with the underlying flow when it rides on a single convection cell; however, the scenario differs remarkably when the leading edge of the plate encounters impeding flow structures. Three coupling modes are identified and elucidated below.

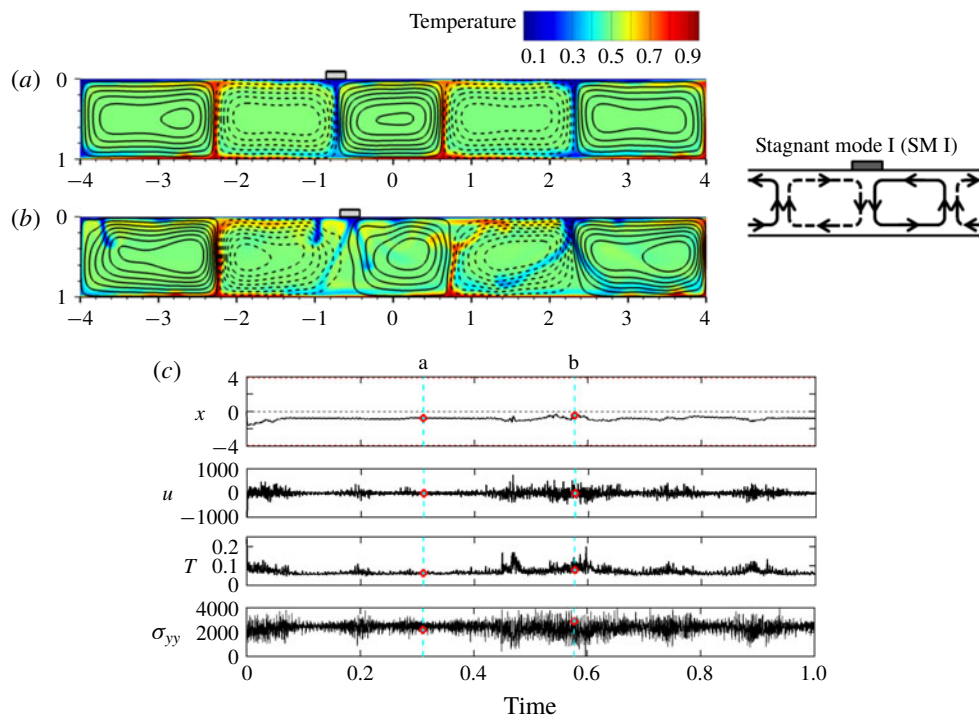


FIGURE 2. Stagnant mode I (SM I) for $L = 0.25$ at $Ra = 10^6$, $h = 0$. (a,b) Snapshots of streamlines and temperature for the quiescent duration and the active duration, respectively, with a sketch of the flow structure of SM I on the right-hand side. The corresponding times are marked in (c) with red circles and cyan lines. The solid and dashed streamlines represent anticlockwise and clockwise flows, respectively. (c) Time series of plate centre location x , plate velocity u , the average temperature T and average normal stress σ_{yy} at plate bottom.

3.1. Stagnant mode I

A small plate is easily trapped when it encounters a downwelling and a counter-rotating convection cell, as the opposing flows of the two cells converge beneath the plate (figure 2a,b). The opposing forces exerted by these opposing flows on the bottom of the plate tend to balance each other by adjusting the plate position. This is a stable mode, since the plate will be pulled back if it is moved slightly away from the balanced position. As a result, the plate is trapped for a long time, which we term stagnant mode I (SM I). For a small plate of $L = 0.25$, it never shows significant displacement after being arrested by the downwelling (figure 2c) and the underlying flow structure remains approximately the same. Nevertheless, the system shows an alternation of quiescence (figure 2a) and activity (figure 2b). The former is characterized by a more regular flow structure (figure 2a) and smaller fluctuations of plate velocity and flow properties with time (figure 2c). Furthermore, during the quiescent duration, the thermal plumes are striking almost vertically towards the opposing boundaries (figure 2a). In contrast, they show significant bifurcation and variation during the active duration (figure 2b).

For a small plate of $L = 0.25$, the two convection cells underlying the plate do not show significant variation in size over time. As the plate becomes larger, its capability

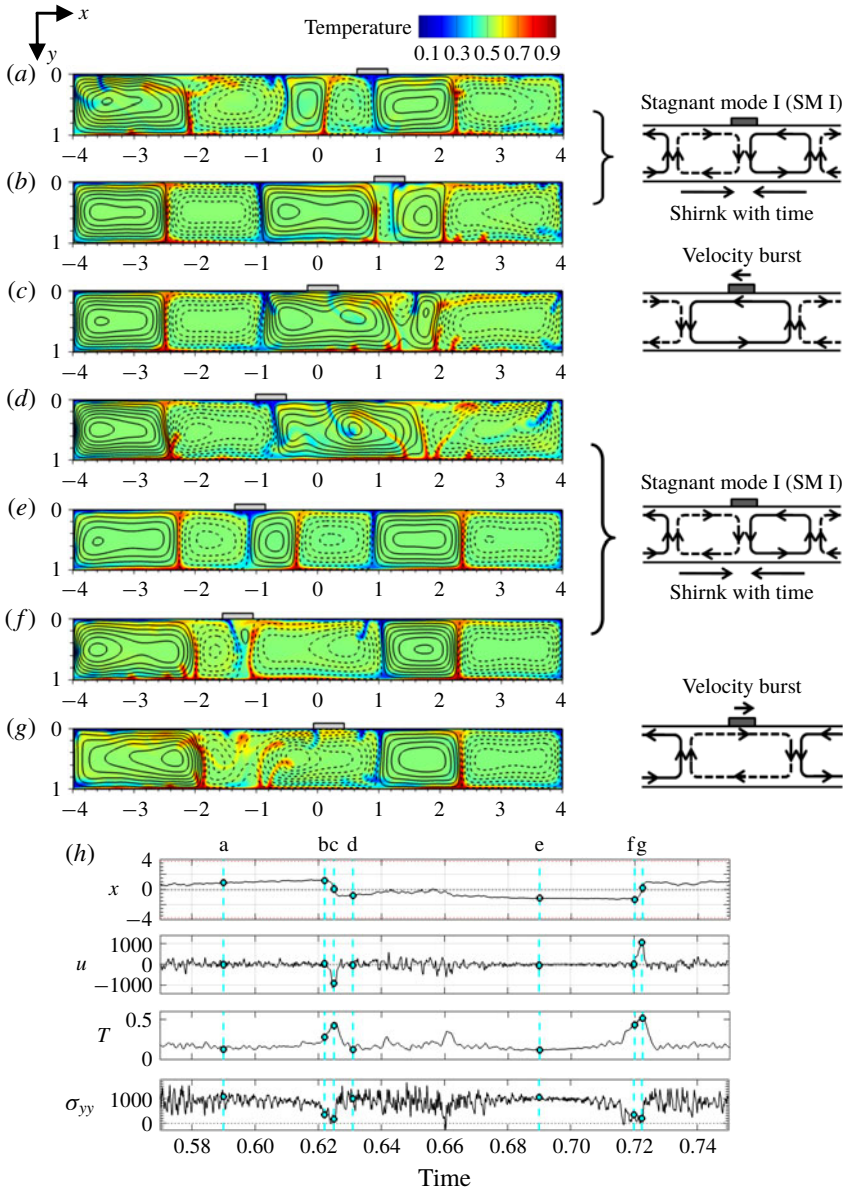


FIGURE 3. Alternation of stagnant mode I (SM I) and velocity bursts for $L=0.5$ at $Ra=10^6$, $h=0$. (a–g) Snapshots of streamlines and temperature with sketches on the right-hand side. (h) Time series of plate centre location x , plate velocity u , average temperature T and average normal stress σ_{yy} at plate bottom.

to modify the flow increases. As a result, as L increases to 0.5, the two convection cells underneath shrink gradually as the two associated hot plumes approach the plate, which is evident by comparing figure 3(a) with 3(b), and figure 3(d) with 3(e) (supplementary movie 1 available at <https://doi.org/10.1017/jfm.2019.189>). Such an evolution of flow pattern is due to the thermal blanket effect as the plate reduces the local heat loss and weakens the downwelling. As the two cells shrink, one of them

eventually vanishes and the remaining one merges with the neighbouring cell of the same sign (this evolution is evident by comparing figure 3*b* with 3*c*, and figure 3*f* with 3*g*), thus the plate rides on a single convection cell and exhibits a burst in velocity (supplementary movie 1). This process of cell vanishing and merging is accomplished when one of the two associated hot plumes reaches the plate. As a result, the bursts in plate velocity are accompanied by evident bursts in temperature T at plate bottom and alleviations of the extensional (positive) normal stress σ_{yy} there (figure 3*h*).

3.2. Stagnant mode II

Another stagnant mode, i.e. stagnant mode II (SM II) (supplementary movie 2), starts to appear at $L \sim 0.75$ and gradually becomes dominant at $L \sim 1.5$. For $L = 1.5$, the plate rides on a single convection cell most of the time (for example, figure 4*a,e,h*). However, plate motion can be severely hindered when the leading edge of the plate encounters a counter-rotating cell and the associated downwelling. As the plate slows down and becomes stagnant, a new downwelling starts to form at the other end of the plate and a hot plume develops underneath, initiating two counter-rotating convection cells underneath and a divergent flow at plate bottom (figure 4*b,f*, supplementary movie 2). The two cells underlying the plate together with the neighbouring cells on each side of the plate form a flow structure that traps the plate, which we term stagnant mode II (SM II). This is a stable structure, since a minor shift of the plate position will be inhibited by the opposing flow of the neighbouring cell.

Under the insulating plate, the hot plume grows and the two convection cells expand. Meanwhile, the neighbouring hot plume on each side of the plate moves towards the plate. As a result, the two underlying convection cells merge respectively with the nearest cell of the same sign on each side of the plate at the cost of a counter-rotating cell, which is evident by comparing figure 4(*c*) with 4(*d*), and figure 4(*f*) with 4(*g*) (supplementary movie 2). This is contrary to the shrinkage of the underlying cells in SM I. Nevertheless, SM II becomes unstable when the two underlying cells merge with the neighbouring cells and become large (figure 4*d,g*), since a small shift of the plate position will be amplified rather than inhibited as in SM I. One of the two cells soon becomes dominant in moving the plate and thus the plate rides on a single cell again (figure 4*e,h*), ending its stagnant state. Since the downwelling which initially slows down the plate tends to drag the plate downwards, the decrease in plate speed u owing to the encounter of downwelling is accompanied by an increase in the extensional stress σ_{yy} at the plate bottom, and a decrease in the average temperature T there (figure 4*i*). Conversely, during the stagnant duration, the growth of hot plumes underneath the plate leads to a gradual increase of T and a decrease of σ_{yy} (figure 4*i*). As the insulating effect of the plate increases with its size, a larger plate needs a shorter time to warm up the underlying flow and modify the underlying flow structure. Therefore, SM II is much shorter-lived than SM I.

3.3. Unidirectional moving mode

As the plate size increases to $L = 2.5$, the aforementioned two stagnant modes disappear and the unidirectional moving mode (UMM) emerges (supplementary movie 3). In this mode, the plate rides most of the time on a single large convection cell and moves unidirectionally until it encounters the end walls (figure 5), where it is forced to stop until hot plumes rise up underneath and the net underlying horizontal flow reverses (figure 5*d*), similar to that observed by Whitehead & Behn (2015).

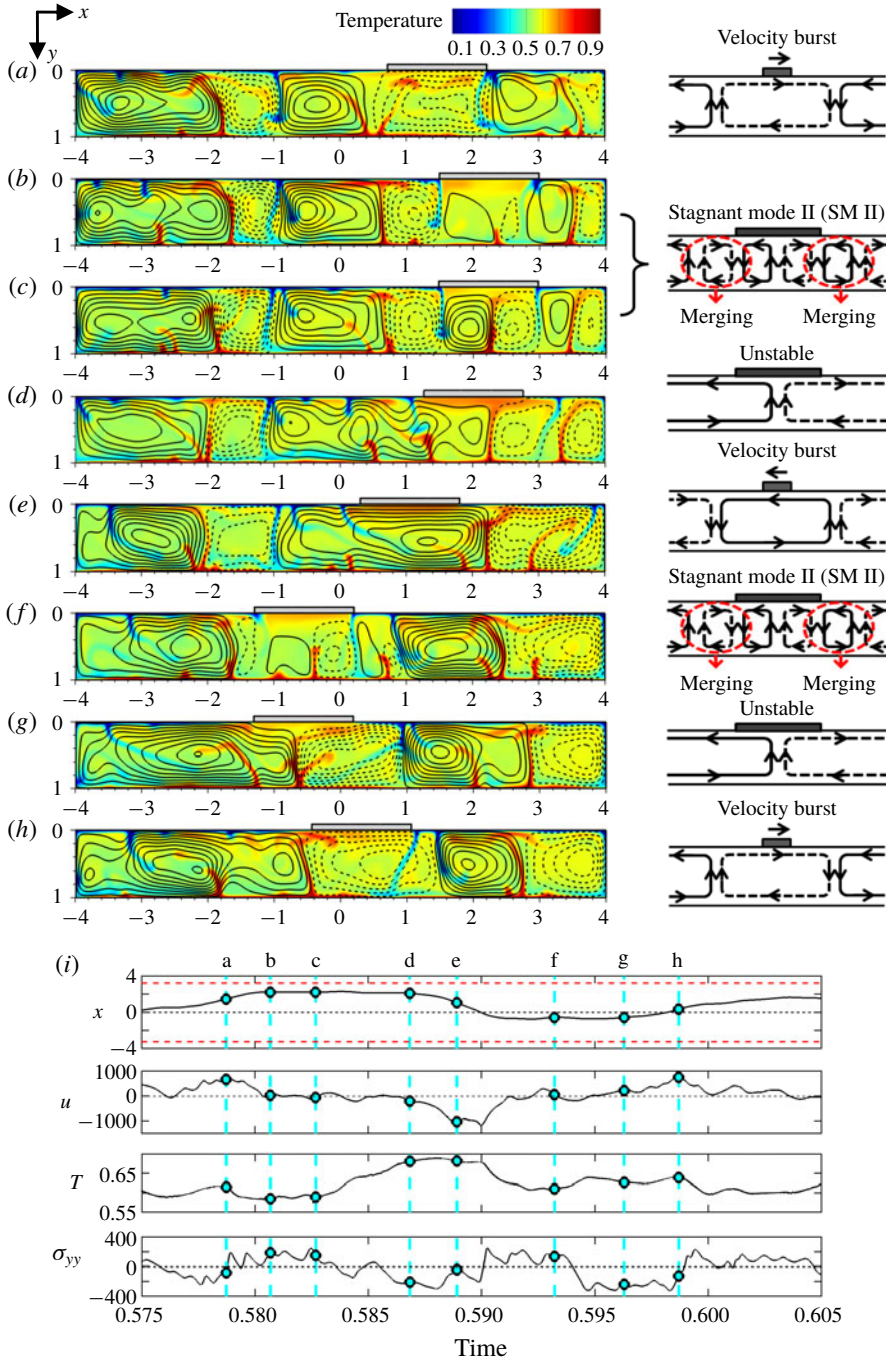


FIGURE 4. The evolution of stagnant mode II (SM II) for $L = 1.5$ at $Ra = 10^6$, $h = 0$. (a–h) Snapshots of streamlines and temperature with sketches of flow structure on the right-hand side. (i) Time series of plate centre location x , plate velocity u , average temperature T and average normal stress σ_{yy} at plate bottom.

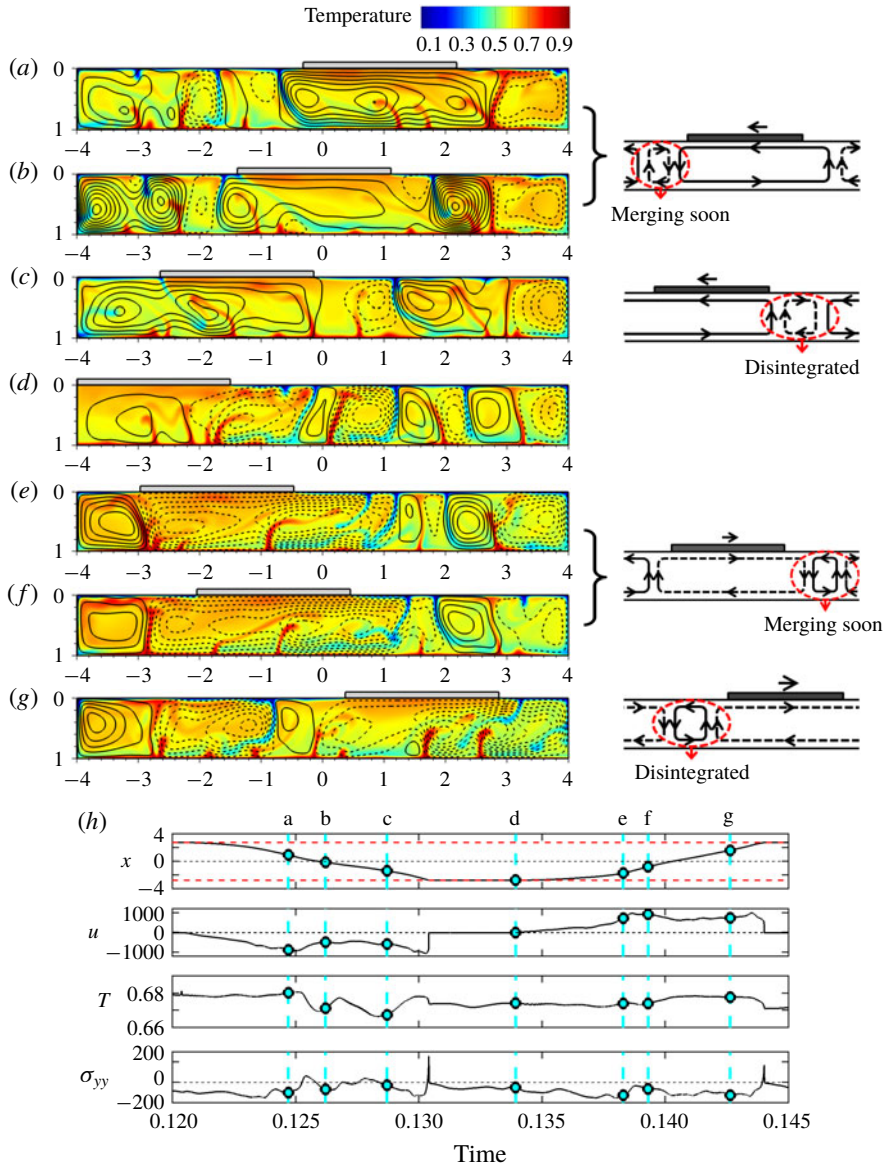


FIGURE 5. The unidirectional moving mode (UMM) for $L = 2.5$ at $Ra = 10^6$, $h = 0$. (a–g) Snapshots of streamlines and temperature (UMM) with sketches of flow structure on the right-hand side. (h) Time series of plate centre location x , plate velocity u , average temperature T and average normal stress σ_{yy} at plate bottom. Except moments of forced stop in (d), a single large convection cell is always identified underlying the plate.

the leading edge of the plate encounters a cold downwelling, instead of being stopped as in the stagnant modes, the plate slows down transiently but continues moving forwards, taking the cold plume along with it (supplementary movie 3). Meanwhile, the underlying convection cell merges with the frontal cell of the same sign, at the cost of a counter-rotating cell, which is evident by comparing figure 5(a) with 5(b), and figure 5(e) with 5(f). On the other hand, when the underlying convection cell becomes large through merging, it disintegrates by forming new hot upwelling near

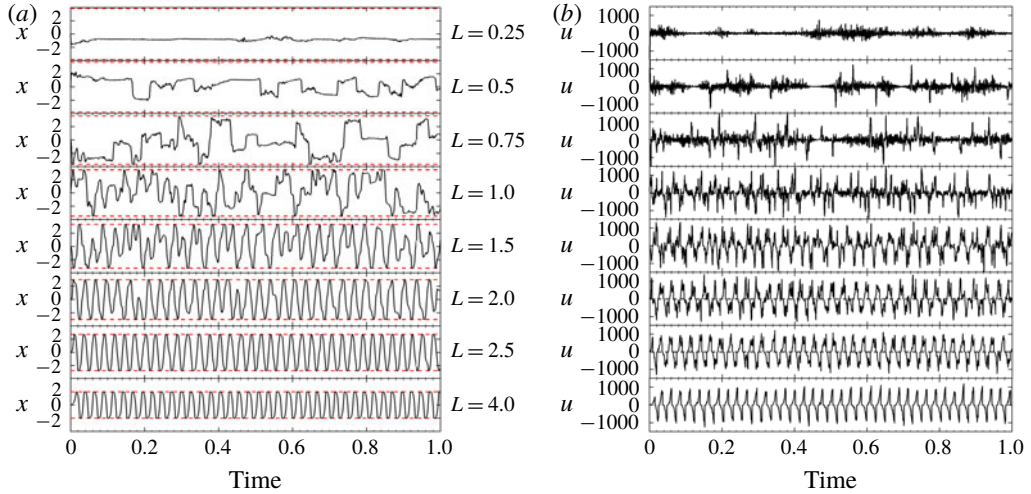


FIGURE 6. (a) Plate centre position x and (b) plate velocity u for $Ra = 10^6$, $h = 0$. Time starts from when the plate is freed. The red horizontal lines denote the maximum range of plate centre position x .

the trailing edge of the plate, which is evident by comparing figure 5(b) with 5(c), and figure 5(f) with 5(g). Such a process of cell merging near the leading edge and disintegration near the trailing edge continues, resulting in the propagation of a large convection cell with the moving plate (supplementary movie 3).

A comparison of the average normal stress σ_{yy} at the plate bottom among different cases suggests that as plate size increases, the value of σ_{yy} changes from generally positive to generally negative (figures 2–5), suggesting that the plate transfers from being dragged down by cold downwelling to being uplifted by hot upwelling. This is consistent with the generally larger number of hot plumes identified underneath the larger plate (figures 2–5), which embodies the increase of the thermal blanket effect with plate size.

4. Analysis on the simulation results

4.1. Variation of plate speed with plate size

It is clear now that plate motion varies significantly with its size. Very small plates ($L \lesssim 0.25$) are permanently trapped in SM I with no significant displacement once being trapped (figure 6, $L = 0.25$). As plate size increases to $L = 0.5$, the plate shows long durations of stagnancy punctuated by short episodes of velocity burst (figure 6). Excluding the forced stop at the end walls, the duration of stagnancy decreases with increasing plate size (figure 6). For $L \geq 2.5$, the plate shows unidirectional movement until it encounters the end walls (figure 6a, $L = 2.5, 4.0$).

An analysis on the time series of plate speed $|u|$ reveals that as a plate becomes larger, it is less likely to be stagnant and its speed becomes increasingly concentrated on high values (figure 7a), suggesting its increasing capability to overcome impeding flow structures and maintain a steady motion. As L increases to 2.5, the probability of a plate to be stagnant (low speed, for example, $|u| < 100$) approaches zero (figure 7a,b), corresponding to the UMM of large plates. The enhanced moving capability of larger plates is also manifested in the increase of the average plate speed $|u|_{mean}$ with plate size (figure 7c). The standard deviation of plate speed reaches

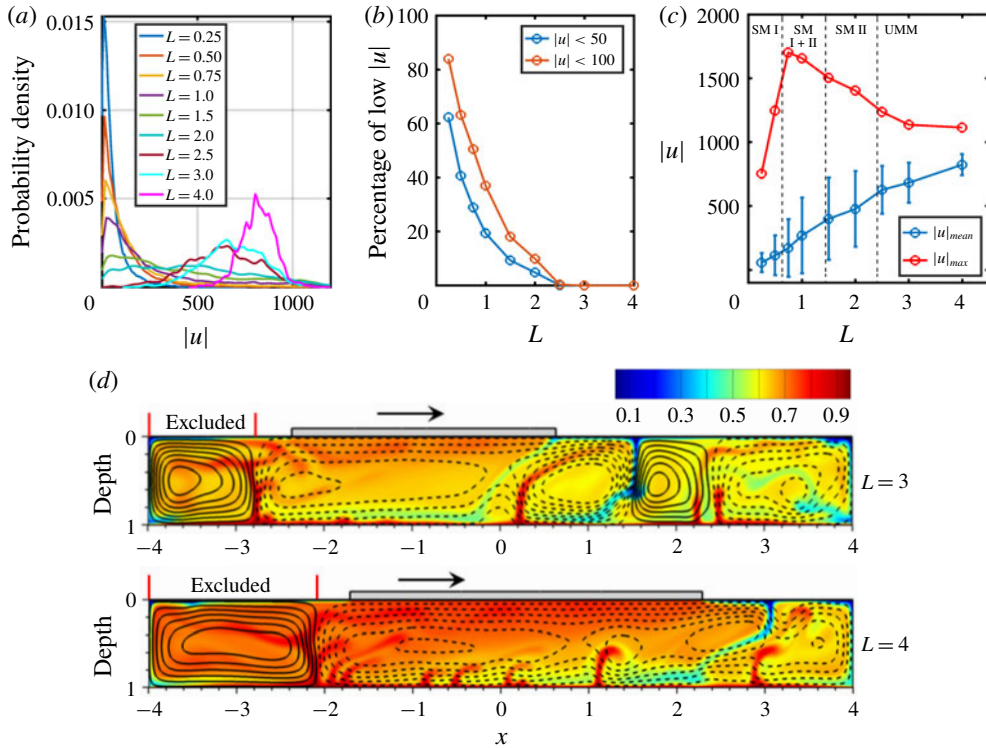


FIGURE 7. Analysis of plate speed $|u|$ for different plate size L at $Ra = 10^6$, $h = 0$ (a) Probability density of plate speed $|u|$. (b) Percentage of low plate speed $|u|$ in the time series of $|u|$. (c) Mean plate speed $|u|_{mean}$ with the standard deviation denoted by the upper and lower bars, and the maximum plate speed $|u|_{max}$. Dashed vertical lines indicate the rough boundaries between different modes (SM I + II denotes a transition from SM I to SM II, where both modes exist). (d) Streamlines and temperature for $L = 3$ (upper panel) and 4 (lower panel) when the plate starts to ride on a single convection cell again after the forced stop at the end wall. The two red lines at the top denote the range of the end-wall cell. Plate speeds affected by this cell are excluded from the analysis.

a maximum at a plate size of $L = 1.5\text{--}2$ (figure 7c). This is because towards the lower end of plate size, the plate shows an increasing tendency to be stagnant, and thus the standard deviation decreases. Towards the upper end, the increasing steadiness of the unidirectional plate motion also results in a decrease of the standard deviation.

The maximum plate speed is reached at a plate size of $L \sim 0.75$ (figure 7c). Since plate speed reflects the average flow speed at the plate–fluid interface, an increase in plate size has the effect of smoothing out local fluctuations and results in more steady plate movement. Therefore, as plate size increases, it is less susceptible to local velocity pulses caused by local flows and thus its maximum speed decreases. On the other hand, a very small plate (e.g. $L = 0.25$) is always trapped in SM I, and therefore its maximum speed is also small. It is worth noting that data at the very initial stage when the plate is just freed are excluded from the above analysis in order to exclude the start-up effect. Furthermore, plate speed affected by the artificially forced stop at the end walls is also excluded, starting from when the plate is forced to stop until it returns back and rides on a single convection cell again (figure 7d). A comparison of

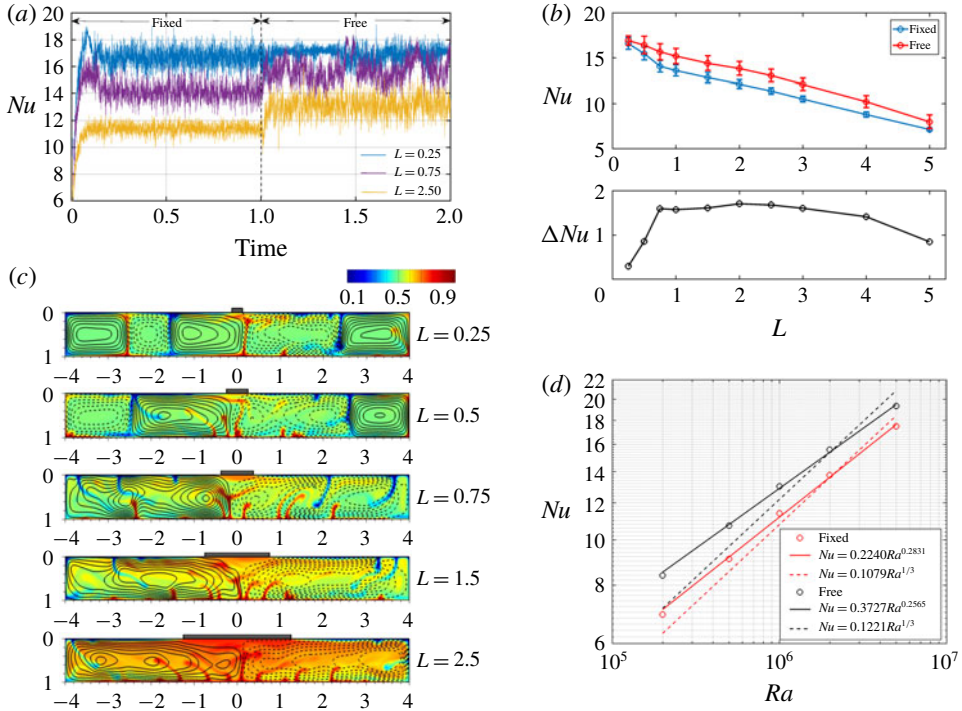


FIGURE 8. (a) Time series of Nu at the bottom of the flow domain for $Ra = 10^6$ and $h = 0$ with fixed and freely moving plates. (b) Time-averaged Nu during the quasi-steady-state at $Ra = 10^6$ for cases with fixed and free plates and their difference (ΔNu). (c) Temperature and streamlines at the quasi-steady-state for cases with a fixed plate. (d) Time-averaged Nu during the quasi-steady-state for $L = 2.5$ at different Ra .

the single convection cell underlying different plates suggests that it becomes larger as plate size increases (figure 7d). For a large plate of $L = 4$, there is not much room left for the development of impeding flow structures for the plate (figure 7d). Therefore, for $L = 4$, the distribution of plate velocity is much more concentrated on relatively high values (figure 7a), showing a rather steady plate movement.

4.2. Comparison of Nu with fixed-plate cases

Compared to cases with a fixed plate, the Nusselt number Nu , increases when the plate is free to move (figure 8a,b). The value of this increase, ΔNu , depends on plate size L , increasing dramatically with L up to $L = 0.75$, staying approximately constant for L ranging from 0.75 to 2.5, and decreasing gradually with L for $L > 2.5$ (figure 8b). Compared to heat transfer by conduction, the thermal plumes that bring fluid from one horizontal boundary straightforwardly towards the opposing boundary present a more efficient means of heat transfer. These thermal plumes are henceforth termed striking thermals since they strike the opposing boundary, in contrast to those short thermals that move fast horizontally with the convective flow until uniting with the striking thermals. Therefore, the presence of a larger number of striking thermals should be associated with a higher efficiency of heat transfer, and hence larger Nu .

For cases with a fixed plate, Nu decreases dramatically with L up to $L = 0.75$ and less abruptly as L continues to increase (figure 8b, blue line). The dramatic decrease

of Nu corresponds to the dramatic decrease of convection cells from five to two, or the associated striking thermals from six to three as L increases from 0.25 to 0.75 (figure 8c). As L continues to increase, the number of convection cells (or striking thermals) becomes constant (figure 8c) and therefore the decrease of Nu with L becomes less abrupt. For $0.75 \leq L \leq 2.5$, only two convection cells, or three associated striking thermals are present for cases with a fixed plate (figure 8c). However, the corresponding cases with a freely moving plate have evidently more convection cells (or striking thermals) (figures 3–5), which lead to a higher efficiency of heat transfer and therefore higher Nu . For large plates of $L > 2.5$, the convection cell underneath the moving plate occupies a large portion of the flow domain (for example, figure 7d). In this case, the space left for the development of other convection cells (or the associated striking thermals) becomes quite limited and it decreases with increasing L (figure 7d). Therefore, as L increases, the number of striking thermals for fixed-plate cases and that for free-plate cases gradually becomes close, and thus ΔNu , the difference of Nu between cases with free and fixed plates, decreases with L for $L > 2.5$. It is expected that ΔNu approaches zero as L approaches the length of the fluid domain.

For a unit square box, the boundary layer theory has predicted a power-law relation of Nu being linearly proportional to $Ra^{1/3}$ (Turcotte & Schubert 2002). Nevertheless, the present configuration is significantly different from a unit square box, not only in the horizontal size of the flow domain but also in the top boundary condition. Therefore, to obtain the Nu – Ra power-law relation ($Nu = \alpha Ra^\beta$) for the case of $L = 2.5$, both the exponent β and the coefficient α are set as the fitting parameters. Our results suggest that the average Nu over the quasi-steady-state scales with $Ra^{0.2831}$ for the fixed-plate cases, and $Ra^{0.2565}$ for the free-plate cases, and therefore the exponents are much smaller than the theoretical value of $1/3$ predicted for a unit square box.

4.3. Variation of plate motion with Ra

For $L = 2.5$, the plate moves unidirectionally under different Rayleigh numbers until it encounters the end wall (figure 9a). Nevertheless, for $Ra = 2 \times 10^5$, the plate motion can still be severely hindered when the plate encounters impeding flow structures (figure 9b). As Ra increases, the probability of low plate speed (for example, $|u| < 100$) decreases significantly, approaching zero for $Ra \geq 10^6$ (figure 9c). Therefore, apart from plate size, the increase of Ra also increases plate capacity to overcome impeding flow structures. Excluding data affected by the end-wall effect, the mean plate speed scales relatively well with $Ra^{2/3}$, which is consistent with the scaling prediction for the mantle flow (Turcotte & Schubert 2002; Grigné, Labrosse & Tackley 2005). However, for $Ra = 2 \times 10^5$, the mean plate speed is evidently lower than the scaling prediction (figure 9d). This is because for this lower Ra , plate movement is often significantly hindered by impeding flow, which counteracts the main flow that drives the plate (figure 9b), and therefore the plate speed is lower than the speed of the underlying flow predicted by the scaling.

4.4. The correlation between plate movement and thermal signals of the flow

The presence of the plate affects the underlying thermal structure, as shown by the isotherms and streamlines in § 3. Further, plate movement or stagnancy can affect the thermal signals of the flow. Some of the thermal signals, including the spatial root mean square temperature T_{rms} , the average temperature \bar{T} over the flow domain, the average temperature \bar{T}_i at the plate–fluid interface and the Nusselt number Nu are shown in figure 10.

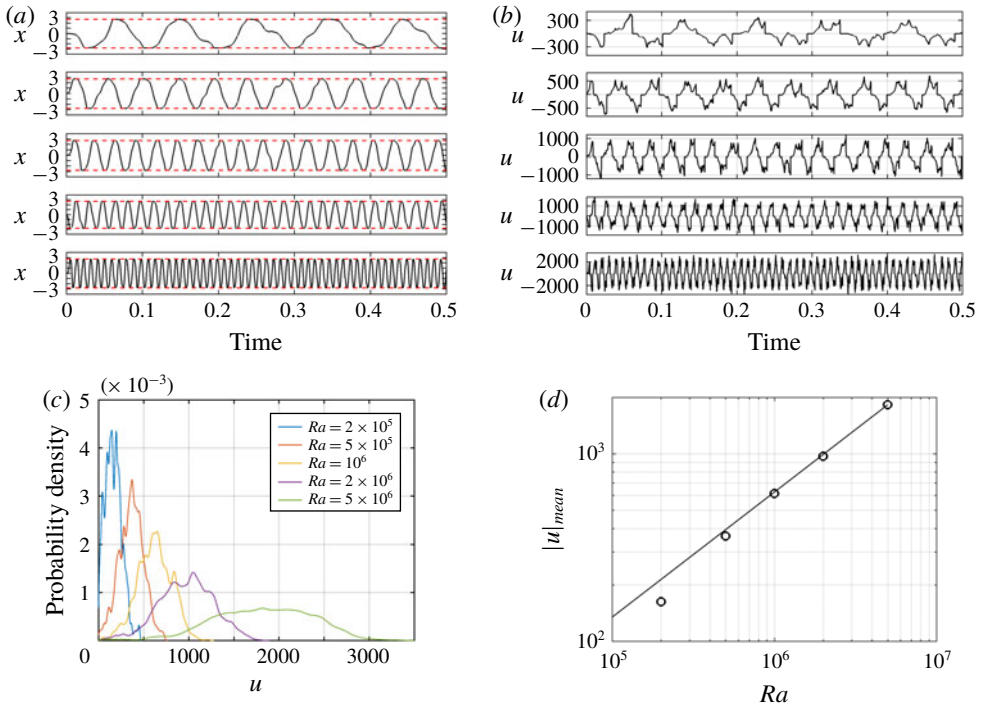


FIGURE 9. Variation of plate motion with Ra for $L=2.5$ and $h=0$. (a) Time series of plate centre location x for $Ra=2 \times 10^5$, 5×10^5 , 10^6 , 2×10^6 , 5×10^6 from top to bottom. (b) Time series of the corresponding plate velocity u . (c) Probability density of plate speed $|u|$. (d) Time-averaged plate speed $|u|_{mean}$ during the quasi-steady-state, the straight line is a fit to the value at $Ra=5 \times 10^6$ and is given by $|u|_{mean} = 0.0627 Ra^{2/3}$.

For a very small plate of $L=0.25$, the quiescent duration (highlighted by the cyan bands in figure 10a) is characterized by lower plate velocity u , lower T_{rms} and higher Nu than the active duration (figure 10a). The lower T_{rms} corresponds to the more regular flow structure during the quiescent duration (figure 2a). The higher Nu during the quiescent duration corresponds to the more straightforward movement of the thermals towards the opposing boundaries. The vertically moving thermals during the quiescent duration bring colder/warmer material to the lower/upper boundary than the bifurcating and inclining thermals during the active duration (figure 2a,b), resulting in a higher efficiency of heat transfer, and therefore higher Nu . Over the quiescent duration, the time series of the average temperature \bar{T} over the flow domain shows a general trend of slow increase and is much smoother than over the active duration (figure 10a). On the other hand, the average temperature \bar{T}_i at the plate–fluid interface exhibits higher values (suggesting weaker downwellings underneath the plate) during the active durations, consistent with the snapshots of temperature (figure 2a,b).

To investigate the effect of a very small mobile plate ($L=0.25$) on the flow pattern underneath, we remove the plate (at time $t=0.47$) after the coupled system reaches a quasi-steady-state. It is found that the quasi-steady-state flow pattern for the no-plate case is similar to the flow pattern for the case with a small plate of $L=0.25$, shown in figure 2(a), in which the flow domain is occupied by five convection rolls of similar size. Nevertheless, for the no-plate case, the differentiation between the active and the

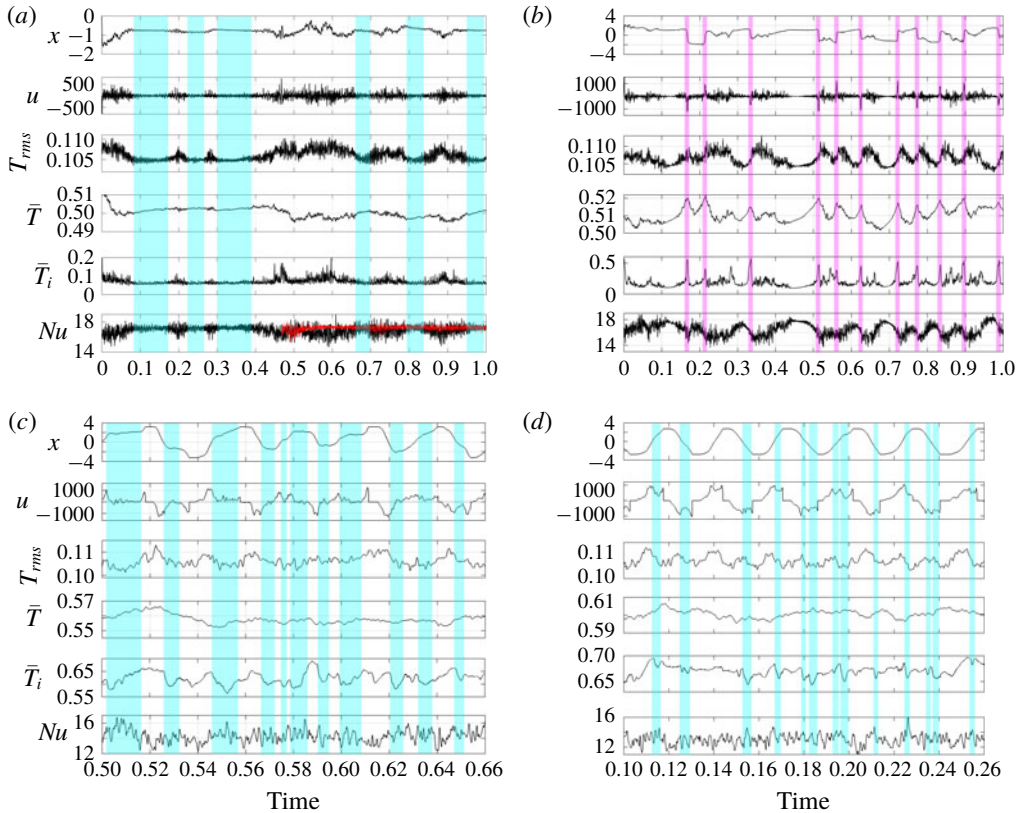


FIGURE 10. The response of thermal signals to plate movement for different plate sizes at $Ra = 10^6$, $h = 0$: time series of plate centre location x , plate velocity u , the spatial root mean square temperature T_{rms} , the average temperature of the flow domain \bar{T} , the average temperature \bar{T}_i over the plate–fluid interface, and the average Nusselt number Nu at the bottom boundary. (a) $L = 0.25$, the cyan bands highlight the quiescent durations, the red line in the time series of Nu shows the result of Nu after the plate is removed at $t = 0.47$. (b) $L = 0.5$, the magenta bands highlight the velocity bursts. (c) $L = 1.5$, the cyan bands highlight the durations when the plate slows down and becomes stagnant. (d) $L = 2.5$, the cyan bands highlight the durations when the plate slows down at first but retains or even increases its speed afterwards.

quiescent duration is less noticeable and the fluctuation of flow properties with time is much smaller, as illustrated by the time series of Nu (red line in figure 10a). Therefore, rather than being a completely passive tracer, the small plate magnifies the fluctuation of flow properties during the active duration and lowers the average Nu .

As plate size increases to $L = 0.5$, the plate experiences long durations of stagnancy on top of cold downwelling until hot upwelling arrives underneath and brings it a velocity burst. As the plate alternates between stagnancy and velocity burst, the thermal signals, including T_{rms} , \bar{T} , \bar{T}_i and Nu , exhibit consistent trend of variation over time (figure 10b). Plate velocity burst is associated with a general increase of T_{rms} , a maximum of \bar{T} , a burst of \bar{T}_i , and a decrease of Nu (highlighted by the magenta bands in figure 10b). Since plate velocity bursts happen when hot upwelling arrives underneath, bursts of plate velocity correspond to bursts of temperature \bar{T}_i at

the interface. When the plate experiences a velocity burst, the position of the plate changes abruptly. Corresponding to this abrupt change, the underlying convection cells undergo a process of reorganization. During this process, the plume pattern becomes less regular and the number of convection cells decreases (figure 3*b,c*). As a result of flow reorganization, bursts of plate velocity correspond to general increases of T_{rms} and general decreases of Nu , as highlighted by the magenta bands in figure 10(*b*). Shortly after the velocity burst, the plate arrives at another downwelling and becomes stagnant again. The thermal plumes and the convection cells reorganize to adjust to the changed plate position. As the process of reorganization goes on, the spatial pattern of convection cells and the associated plumes becomes more regular and the number of convection cells increases (figure 3*d,e*), resulting in a decrease/increase of T_{rms}/Nu . This process of variation in T_{rms} and Nu persists as the plate alternates between stagnancy and velocity burst. Since a stagnant plate accumulates heat underneath more efficiently than a fast moving plate, the burst in plate velocity is associated with the start of a sharp decrease in the average temperature \bar{T} (figure 10*b*). This decrease persists for a while after the plate reaches a new downwelling. After the plate sits on top of the downwelling for a sufficiently long time, its thermal blanket effect becomes evident and the value of \bar{T} begins to increase with time. As a result, the average temperature \bar{T} reaches a maximum around the time when the plate shows a velocity burst, as highlighted by the magenta bands in figure 10(*b*).

As plate size increases to $L \geq 1.5$, the overall shape of thermal plumes becomes more irregular and their movement towards the opposing boundary becomes less straightforward (figures 4 and 5). The alternation between stagnancy (SM II) and movement becomes less distinct and less differentiable. Further, the duration of stagnancy (SM II) is much shorter than that of SM I for smaller plates, leaving a very limited time for the fluid to reorganize and respond to the newly settled plate position. As a result, the variation of the thermal signals of the fluid with plate movement becomes less obvious (figure 10*c*). Nevertheless, a decrease in plate velocity u and its subsequent stagnation are associated with an evident decrease and then a subsequent increase in the average temperature \bar{T}_i at the interface (highlighted by the cyan bands in figure 10*c*). This corresponding variation in plate velocity u and \bar{T}_i is consistent with the temporal evolution of the stagnant mode II. The encounter of cold downwelling at the leading edge of the plate initiates a slowdown of plate velocity and a decrease in \bar{T}_i , which is evident by comparing figure 4(*a*) with 4(*b*), and figure 4(*e*) with 4(*f*). As the plate slows down, it gradually enters into the stagnant mode II and nurtures the growth of hot upwelling underneath the plate (figure 4*b,c*), resulting in an increase of \bar{T}_i at the interface. This variation of \bar{T}_i after the slowdown of plate velocity is also observed for the even larger plate case of $L = 2.5$. As the thermal blanket effect is enhanced with increasing plate size, the decrease and the subsequent increase in \bar{T}_i (highlighted by the cyan bands in figure 10*d*) is completed in shorter durations for the case of $L = 2.5$ than for the case of $L = 1.5$ (figure 10*c,d*). Further, the large plate of $L = 2.5$ slows down when it encounters a cold downwelling, but the plate soon warms up the downwelling, resulting in the decrease of the spatial root mean square temperature T_{rms} with decreasing u . Conversely, an increase of plate velocity from zero, after the forced stop at the end wall, is associated with the generation of hot thermal plumes underneath the plate (figure 5*d*), which is reflected in the increase of T_{rms} as u increases from zero (figure 10*d*).

4.5. The effect of internal heating on plate movement

Apart from bottom heating at the core–mantle boundary, radioactive decay provides an essential heating source for the interior of the Earth (Turcotte & Schubert 2002).

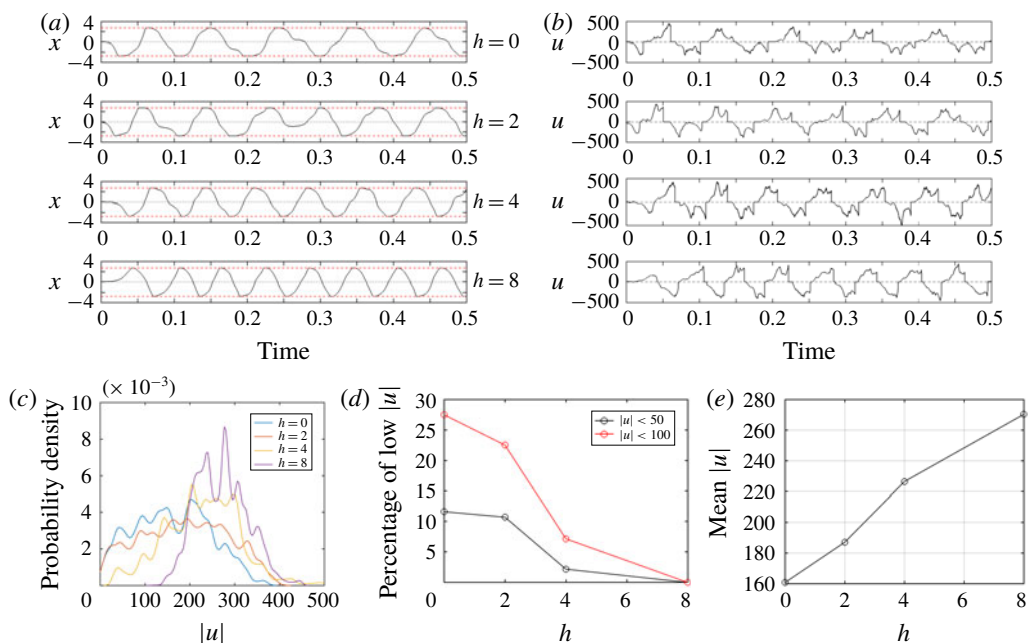


FIGURE 11. The effect of internal heating on plate movement illustrated with a parameter setting of $L = 2.5$, $Ra = 10^6$, $h = 0, 2, 4, 8$. (a) Plate centre position x and (b) plate velocity u for $Ra = 10^6$ and $L = 2.5$ with different internal heating rates, $h = 0, 2, 4, 8$. Time starts from when the plate is freed. The red horizontal lines denote the maximum range of plate centre position x . (c) Probability density of plate speed $|u|$. (d) Percentage of low plate speed $|u|$ in the time series of $|u|$. (e) Time-averaged plate speed $|u|$ during the quasi-steady-state. Data shown in (d,e) exclude those when plate movement is affected by the artificially forced stop at the end wall.

To investigate the effect of internal heating on plate movement, simulations were conducted by applying different intensities of internal heating for the case of $L = 2.5$ (figure 11). Time series of the plate centre position x and plate velocity u show increasing steadiness of plate movement as the intensity of internal heating h increases (figure 11a,b). As h increases, the distribution of plate speed $|u|$ becomes increasingly concentrated on high values (figure 11c), suggesting an increasing steadiness of plate movement and an increasing overall plate speed. Meanwhile, as h increases, the probability and the percentage of low plate speed decrease (figure 11c,d), suggesting a decreasing likelihood of plate movement being severely hindered by impeding flow structures. The average plate speed $|u|$ increases with increasing h (figure 11e). Therefore, plate mobility or its capability to overcome impeding flow structures increases with increasing internal heating intensity h .

A comparison was also made between one case with $h = 0$ (no internal heating) and another one with $h = 8$ for a small plate size of $L = 0.5$. Time series of plate centre position x and plate velocity u show that plate mobility increases significantly as internal heating is switched on (figure 12a). For $h = 8$, as a result of the enhanced plate mobility, the distinction between stagnation and velocity burst becomes less differentiable in the times series of plate velocity u , and the plate is able to reach the end walls (figure 12a). Consequently, the probability of plate stagnation (low plate speed $|u|$) decreases significantly as h increases from 0 to 8 (figure 12b).

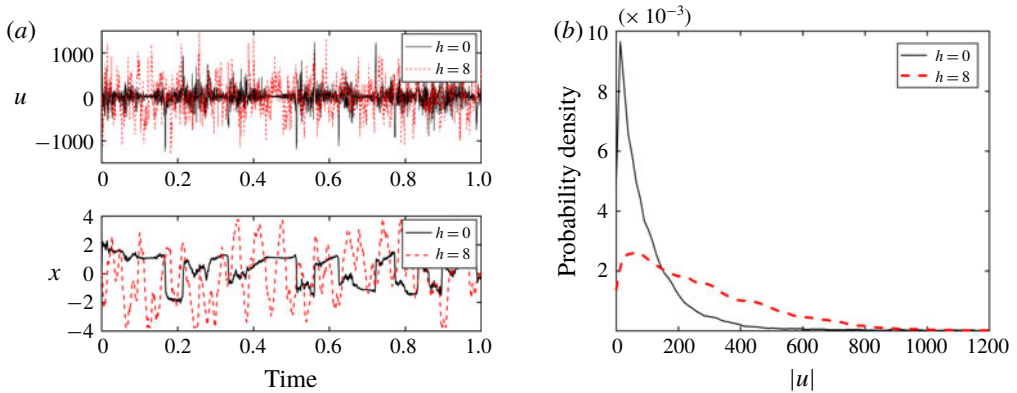


FIGURE 12. The effect of internal heating on plate movement illustrated with a parameter setting of $L=0.5$, $Ra=10^6$, $h=0, 8$. (a) Plate centre position x and plate velocity u for $Ra=10^6$ with $h=0$ (black line) and $h=8$ (red dashed line). Time starts from when the plate is freed. (b) Probability density of plate speed $|u|$.

4.6. The presence of different modes in three dimensions

To illustrate the presence of different modes in three dimensions, 3-D simulations were conducted in a $8 \times 8 \times 1$ (8×8 is the horizontal dimensional size and 1 is the depth) convective domain with a square plate of different sizes floating on top of it. Although the plate is set free to move from the beginning when the entire flow is isothermal and stationary, it is observed that all of the plates remain stagnant at the initial stage and only begin to move at a more developed stage.

The addition of a new dimension in space introduces much richer dynamics in the fluid domain and more possibilities in plate movement. Nevertheless, the three different coupling modes (SM I, SM II and UMM) revealed in two dimensions are all identified in three dimensions, and the basic characteristics of the different modes are consistent with those observed in two dimensions.

For a small plate with a horizontal size of 0.5×0.5 , the plate shows a short episode of velocity burst when its underlying flow is coherently flowing in one direction, from a site of hot upwelling towards a site of cold downwelling (figure 13*a,d*). When the plate arrives at the site of downwelling, the underlying flow converges underneath the plate and flows downwards towards the bottom of the fluid domain. The convergence of flow underneath the plate involves flows in two opposing directions for the 2-D cases (figures 2*a*, 3*a,e*), but involves flows in all horizontal directions for the 3-D case (figure 13*b,c*). The coupled system achieves a balance by adjusting the plate position so that the forces exerted by the underlying flow on the plate are balanced. This is a stable mode since the plate will be pulled back to the balanced position if it is moved slightly away from it. Figure 13(*b*) shows the snapshot of two isothermal surfaces and streamlines of SM I at an early stage of flow development, while the presence of SM I at a more developed stage is illustrated in figure 13(*c*). The convergence of flow underneath the plate is shown by the streamlines there, and the presence of cold downwelling at the plate position is demonstrated by the translucent blue isothermal surface.

For a larger plate with a horizontal size of 1.5×1.5 , the presence of SM II is illustrated in figure 14. Figure 14(*a*) shows the snapshot of isothermal surfaces and streamlines when the fluid underneath the plate flows almost coherently in one

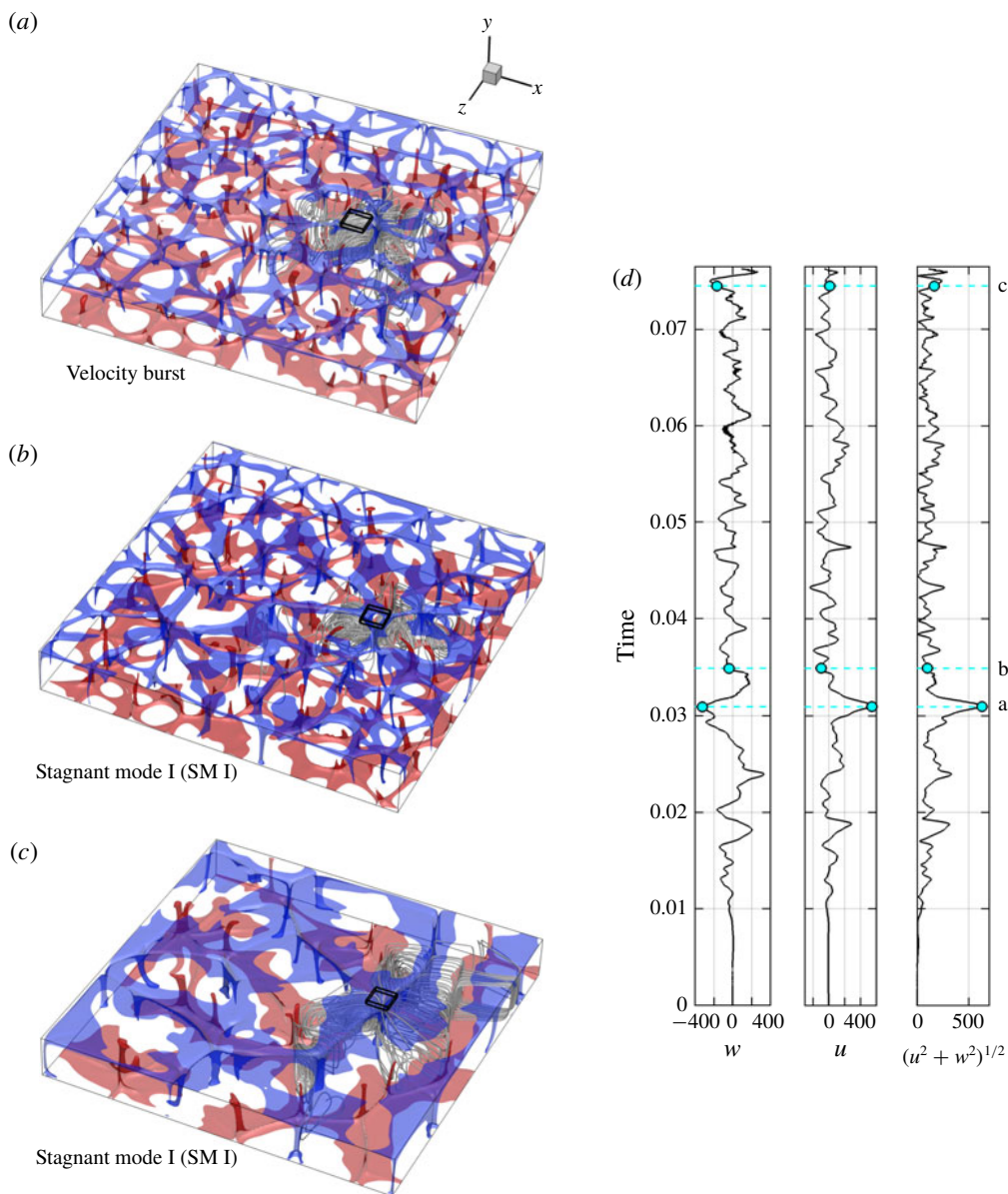


FIGURE 13. The evolution of stagnant mode I in three dimensions with a plate size of 0.5×0.5 , $Ra = 10^6$ and $h = 0$. The translucent blue and red iso-surfaces represent isothermal surfaces of 0.25 and 0.8, respectively. The grey lines represent streamlines around the plate. (a–c) are snapshots of isothermal surface and streamlines. (a) Corresponds to a time when plate shows velocity burst. (b,c) Correspond to the time when the plate shows SM I at an early and a more developed stage respectively. (d) Time series of plate velocity components, u , w and its horizontal speed $(u^2 + w^2)^{1/2}$. The corresponding times of (a–c) are marked with cyan dots and lines in (d).

direction, nearly parallel to the z axis. It is about to encounter flows in different directions at its leading edge. As the plate moves ahead, the coherent flow structure underneath the plate disappears and the plate slows down. This slowing down of

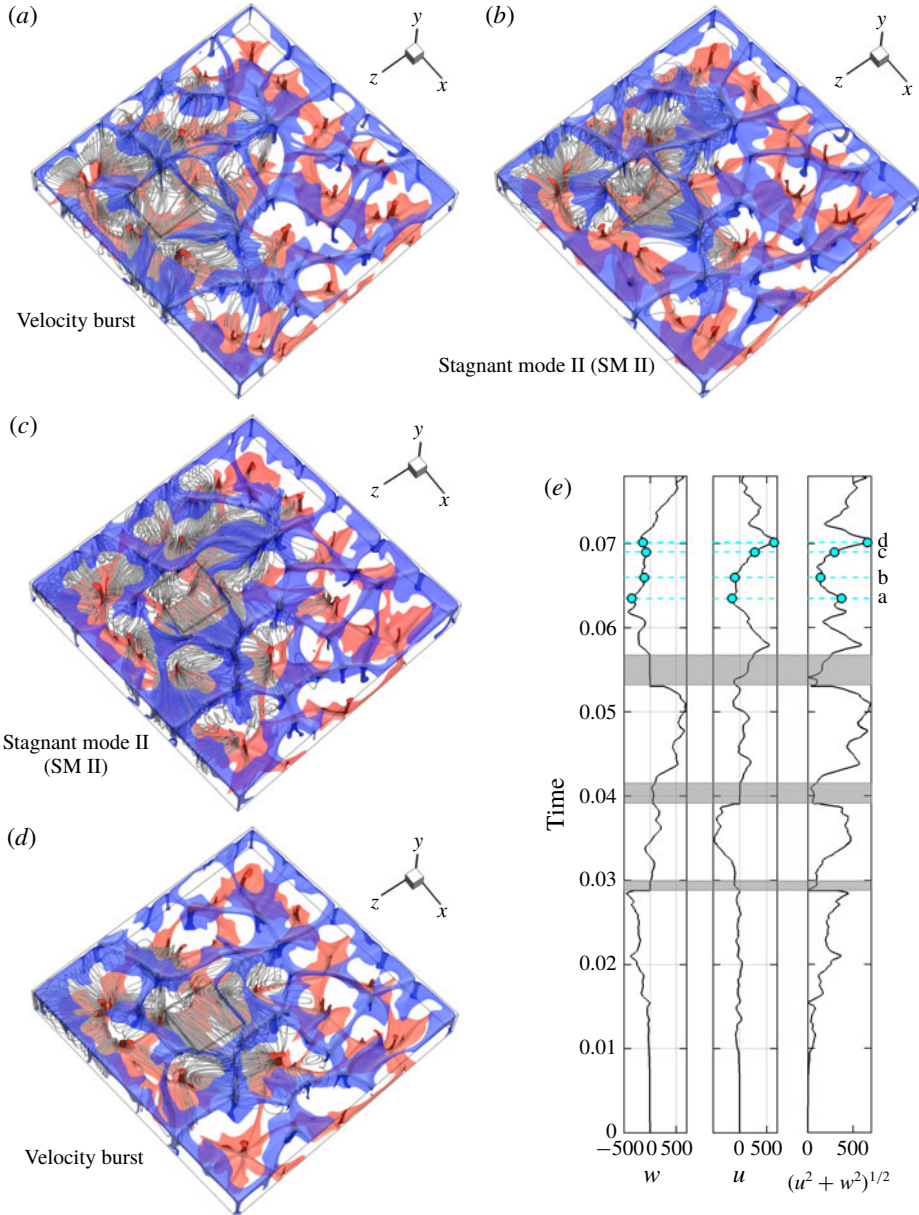


FIGURE 14. The evolution of stagnant mode II in three dimensions with a plate size of 1.5×1.5 , $Ra = 10^6$ and $h = 0$. The translucent blue and red iso-surfaces represent isothermal surfaces of 0.25 and 0.8, respectively. The grey lines represent streamlines around the plate. (a–d) Snapshots of isothermal surface and streamlines. (a) Corresponds to the time when the plate shows velocity burst. (b) Corresponds to the time when plate begins to show SM II. (c) Corresponds to the time when the SM II is about to end. (d) Corresponds to the time when the plate shows velocity burst again. (e) Time series of plate velocity components, u , w and its horizontal speed $(u^2 + w^2)^{1/2}$. The corresponding times of (a–d) are marked with cyan dots and lines in (e). The grey bands mark the duration when plate velocity is affected by the end wall, i.e. the plate is not allowed to penetrate the end wall.

plate enhances the thermal blanket effect of the plate to the underlying flow and nurtures the growth of hot thermal plumes underneath the plate. Consequently, a hot plume starts to rise up underneath the plate (figure 14*b*), similar to the 2-D case (figure 4*b,f*). The presence of the hot plume underneath the plate gives a divergent flow structure there, as shown by the streamlines (figure 14*b*), analogous to the 2-D case (figure 4*b,f*). As the plume grows and the underlying flow evolves with time, the flow in the direction parallel to the positive x axis starts to become dominant (figure 14*c*), and the plate is about to move in the same direction as the dominant flow. Figure 14(*d*) shows the termination of SM II, in which the plate rides on a coherent flow again, almost parallel to the positive x axis. During this evolution of SM II, the plate changes its direction from originally moving parallel to the z axis before the stagnation mode to moving parallel to the x axis after the stagnation mode, as illustrated by the direction of streamlines in figure 14(*a,d*). This change of direction is also evident in the time series of velocity components, in which the w component decreases and the u component increases during the evolution of SM II (figure 14*e*).

For an even larger plate with a horizontal size of 2.5×2.5 , the presence of the unidirectional moving mode is illustrated in figure 15. The plate is observed to move almost straightforwardly until it encounters the end wall. Figure 15(*a*) shows the snapshot when the plate rides on a coherent flow structure and is about to encounter impeding flow structure at its leading edge. Hot thermals are observed to rise up at its trailing edge while cold downwellings occur close to its leading edge, similar to the pattern of a single underlying convection cell in the 2-D case. When the plate encounters the downwelling and the associated impeding flow structure at its leading edge, it slows down but continues its movement forwards, taking the cold downwelling along with it (figure 15*b*). As a result, the cold downwelling is observed to dip at an angle beneath the moving plate, similar to the 2-D case (figure 5*b*). This slowing down of plate enhances the thermal blanket effect of plate to the underlying flow and the underlying flow quickly readjusts by forming new uprising hot plumes which are observed at a later stage (figure 15*c*). The underlying flow quickly reorganizes by merging with the frontal flow of the same direction and disintegrating at the trailing edge of the plate. As a result of this reorganization, the plate rides on top of a strong coherent flow again and resumes its fast motion (figure 15*c*). This process of flow merging at the leading edge and disintegrating near the trailing edge is consistent with that observed in the 2-D case (figure 5).

The time series of plate centre position is shown in figure 16. While a small plate (0.5×0.5) remains almost in the same position after a velocity burst, larger plates (1.5×1.5 , 2.5×2.5) show increased mobility. As the flow develops to a relatively mature stage, the largest plate (2.5×2.5) shows almost a unidirectional movement until it encounters the end wall. Whereas the medium plate (1.5×1.5) detours during its movement, since it is easily affected by the flow structure it encounters and changes its direction afterwards (figure 14). These characteristics of plate movement agree with the time series of velocity components (figures 13*d*, 14*e*, 15*d*) and are consistent with the characteristics of plate motion in the corresponding 2-D cases.

5. Discussions and conclusions

Plate size is revealed to have a strong influence on its motion over a thermally convecting fluid. A small plate, with a weak capability to modulate the underlying flow, easily falls into stagnancy when encountering impeding flow structures, whereas a

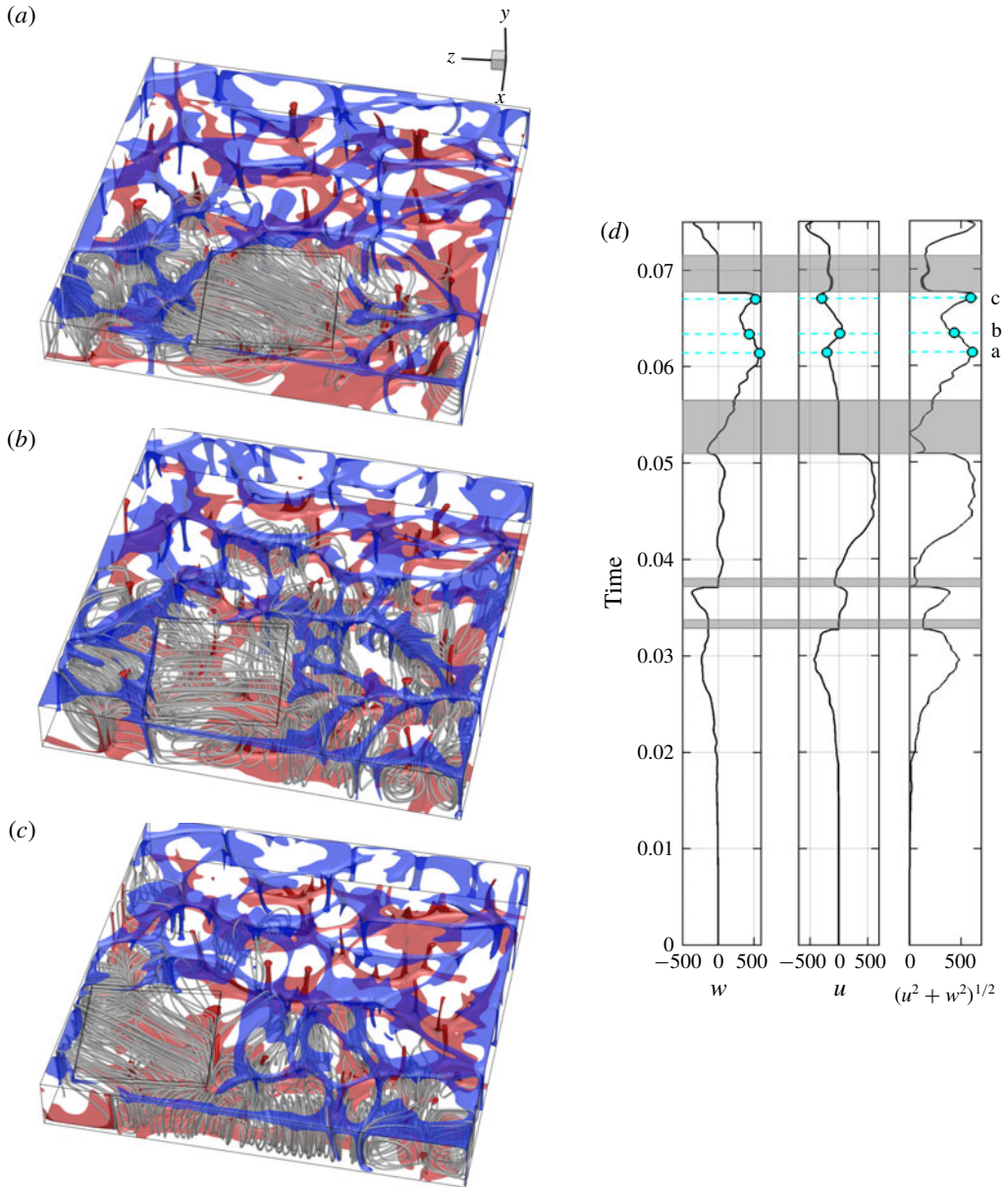


FIGURE 15. The unidirectional moving mode (UMM) in three dimensions with a plate size of 2.5×2.5 , $Ra = 10^6$ and $h = 0$. The translucent blue and red iso-surfaces represent isothermal surfaces of 0.25 and 0.8, respectively. The grey lines represent streamlines around the plate. (a–c) Snapshots of isothermal surface and streamlines. (a) Corresponds to the time when the plate is about to encounter impeding flow. (b) Corresponds to the time when the plate slows down after it encounters downwelling. (c) Corresponds to the time when the underlying convective flow reorganizes and the plate resumes its velocity. (d) Time series of plate velocity components, u , w and its horizontal speed $(u^2 + w^2)^{1/2}$. The corresponding times of (a–c) are marked with cyan dots and lines in (d). The grey bands mark the duration when plate velocity is affected by the end wall, i.e. the plate is not allowed to penetrate the end wall.

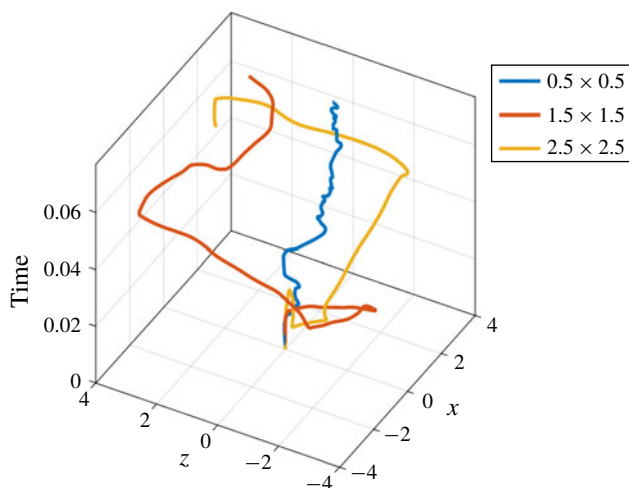


FIGURE 16. Time series of plate centre position x, z with three plate sizes of 0.5×0.5 , 1.5×1.5 , 2.5×2.5 , $Ra = 10^6$ and $h = 0$.

large plate ($L \geq 2.5$) quickly modifies the impeding flow and moves unidirectionally along with a single convection cell underneath it. As a plate becomes larger, it becomes less likely to be stagnant. Two stagnant modes are identified, i.e., SM I and SM II, characterized by the presence of cold downwelling and hot upwelling underneath the plate, respectively, corresponding to convergent and divergent underlying flow, respectively. For $Ra = 10^6$, the plate is permanently trapped in SM I for $L \leq 0.25$. As L increases to 0.5, the plate experiences an alternation of SM I and velocity bursts. A small plate gradually escapes from SM I as the two underlying convection cells shrink and the neighbouring hot plumes move towards it. As L increases to 0.75, SM II starts to appear and this mode becomes dominant in trapping the plate at $L = 1.5$. The plate escapes from SM II as the underlying hot plume grows and the neighbouring hot plumes move towards it. This results in the merging of underlying convection cells with the neighbouring cells and thus the enlargement of the two underlying cells, which is contrary to their shrinkage in SM I. For $L \geq 2.5$, the plate moves unidirectionally by quickly modifying impeding flow structures on its way. As a result, a single convection cell is maintained underneath the plate, merging with frontal cells of the same direction and disintegrating at the back as the plate moves ahead. Although the possibilities of plate movement and flow dynamics in three dimensions are much richer than in two dimensions, the coupling modes between the plate and the underlying fluid are essentially the same. The three coupling modes revealed in two dimensions, namely SM I, SM II and UMM, are all identified in three dimensions.

Although the present simplified model is far from representing Earth itself, the identified coupling modes are reminiscent of some real Earth cases. While most continents have been moving from geoid highs to geoid lows along with the underlying mantle flow since the breakup of Pangaea approximately 170 Myr ago (Turcotte & Schubert 2002), some have been rather stagnant. One of them is the African continent, which has been staying roughly stationary in a deep mantle plume reference frame since the breakup of Pangaea (Burke & Torsvik 2004; Torsvik *et al.* 2008, 2010). It is being uplifted by a huge mantle plume (hot upwelling) in the

eastern and southern part (Ebinger & Sleep 1998; Ritsema, van Heijst & Woodhouse 1999), and high velocity anomalies, which correspond to cold downwelling, were identified near the edge of the continent (Ritsema *et al.* 1999). This thermal structure conforms to SM II. The average width of the African continent is $\sim 1.2D$ (D is the mantle depth, which is approximately 2900 km) from the middle towards its southern part and $\sim 1.8D$ in the northern part, both of which fall into the size range for the occurrence of SM II (figure 6c). Another stagnant continent, Zealandia, i.e. the largely submerged continent of New Zealand, has been straddling the oceanic subduction site at the Pacific–Australia plate boundary since its arrival there 25 Ma ago (Sutherland 1999; Cande & Stock 2004). As a subduction site corresponds to cold downwelling, the thermal structure of the mantle flow underneath Zealandia is reminiscent of SM I. The average width of Zealandia is approximately $0.4D$, which falls into the size range for the occurrence of SM I, as suggested by the above simulation results (figure 6c). Interestingly, these two stagnant continents are associated with extreme elevation anomalies. Over 90% of Zealandia is below water (Suggate, Stevens & Te Punga 1978), whereas the southern and eastern African plateau stands more than 1 km above sea level (Lithgow-Bertelloni & Silver 1998). These elevation anomalies suggest that Zealandia is being dragged down by cold downwelling, whereas the African continent is being uplifted by hot upwelling, correlating well with the positive (extensional) and the negative (compressional) vertical normal stress σ_{yy} identified at the plate bottom for SM I (figure 2g) and SM II (figure 3i), respectively.

The Earth system is much more complex than the present oversimplified model. Several other factors should be taken into account when applying the present results to the Earth itself. First, the present study is conducted at a Rayleigh number of $Ra = 10^6$, which is still on the lower end of Rayleigh number for mantle convection. For an estimation of the Rayleigh number for the mantle, the following parameters are taken from Turcotte & Schubert (2002), a thermal diffusivity of $\kappa = 10^{-6} \text{ m}^2 \text{ s}^{-1}$, a dynamic viscosity of $\mu = 10^{21} \text{ Pa s}$, a thermal expansion coefficient of $\beta = 3 \times 10^{-5} \text{ K}^{-1}$, an average density of $\rho = 4000 \text{ kg m}^{-3}$, a temperature difference of $\Delta T = 2900 \text{ K}$ and a mantle depth of $D = 2880 \text{ km}$, resulting in a Rayleigh number of approximately 8×10^7 . Nevertheless, this value is associated with uncertainties, largely because of the uncertainties in the value of viscosity, which is temperature- and pressure-dependent and varies significantly with depth (Turcotte & Schubert 2002). While the viscosity of the upper mantle is of the order of 10^{21} Pa s (Mitrovica 1996), several geoid studies, which are reviewed in King (1995), have suggested a viscosity jump by a factor of approximately 30 for the lower mantle. Using the high viscosity value of the lower mantle in the calculation of Ra would decrease the above Ra value by a factor of 30. If the detailed radial profile of viscosity was known, an effective Rayleigh number could be calculated using the volume average of viscosity. Moreover, for the layered mantle convection model, a much lower Ra is expected for the upper mantle convection, as the values of both ΔT and the depth of the fluid layer D are much smaller than those for the whole-mantle convection model. For instance, a value of 2.55×10^5 has been estimated by Jarvis & Peltier (1989) as the Rayleigh number for the upper mantle convection. In fact, a wide range of values, from $\sim 10^5$ to $\sim 10^9$, with most falling into the range 10^5 – 10^8 , have been adopted as the Rayleigh number in numerical simulations of mantle convection induced by bottom heating. The selection of a relatively low Ra value is sometimes dictated by computational considerations, since cases with lower Ra are usually less time-consuming. The above discussion of Ra values is concerned with mantle convection subject to pure bottom heating. On the other hand, the Rayleigh number defined for mantle convection subject to pure

internal heating ranges from $\sim 10^6$ for the upper mantle convection and $\sim 10^9$ for the whole mantle convection (Turcotte & Schubert 2002). Since the mantle of the Earth is subject to both bottom heating and internal heating, further studies on the coupling modes are worth pursuing using a model that adopts both thermal forcings, with a proportion that is close to the Earth.

Our simulation results for $L = 2.5$ under various Ra indicate that plates are less likely to be stagnant as Ra increases. It would be interesting to conduct simulations at higher Ra and investigate the effect of Ra on the transition of different modes and the distribution of plate speed. It has been revealed that the horizontal length of the convection cell increases with Ra (Grigne, Labrosse & Tackley 2007). Therefore, for cases with larger Ra , it is expected that a plate will travel longer distances before being impeded and there will be fewer impeding flow structures within the flow domain.

Second, the present study focuses on the influence of a single continent. In reality, continents of different sizes are simultaneously modulating the mantle flow and thus affecting the velocity of each other, and they sometimes break or collide with each other. Therefore, one must be cautious when applying the present evolution of different modes to real continents. Nevertheless, SM I provides a possible mechanism for continent accretion. As it takes a long time for a small continent to escape from stagnancy by itself, other continents may collide and amalgamate with it before it generates a velocity burst by itself. Conversely, SM II promotes continent breakup. In SM II, the evolution of a divergent mantle flow underneath the continent is analogous to that after continent collision, in which hot plumes develop underneath the supercontinent and stay underneath it until continent breaks up and disperses away with the divergent convection flow (Lowman & Jarvis 1993, 1995). Furthermore, the specified forced stop of a plate at the end of the flow domain is analogous to the cessation of movement when continents collide. The flow development afterwards is also characterized by hot plumes rising up underneath the continent and the generation of a divergent flow (figure 4*d*). For future investigations, modelling with a periodic boundary condition at the vertical boundaries is worth pursuing, in which the fluid and the part of the plate passing through one side of the flow domain automatically reappear on the opposite side with the same velocity.

In the present study, oceanic regions are differentiated from the continental regions by a prescribed isothermal free-slip boundary condition. Although this approach is adopted in many mantle convection studies, since oceanic plate can subduct into the mantle and is often regarded as an integral part of mantle convection, it neglects the influence of the rigidity of oceanic plates on mantle convection. In fact, many studies have shown that the presence of large plates significantly influences the thermal structure of the mantle (Bunge & Richards 1996; Zhong *et al.* 2000; Lowman, King & Gable 2001; Monnereau & Quéré 2001). Rigid plates are revealed to control the scale or the dominant wavelength of thermal structures (Davies 1988; Zhong *et al.* 2000). The structure of rigid oceanic plates lying over the soft asthenosphere is expected to induce larger convection cells than in the present model. Moreover, owing to the rigidity of the oceanic plate, continents will encounter higher resistance during their movement, which needs to be taken into account for a more realistic representation. Nevertheless, the existence of the different coupling modes revealed in the present study is unlikely to be affected by the rigidity of oceanic plate.

Results show that an increase in the intensity of internal heating results in an increased mobility of plate. Therefore, plates will be less stagnant and more mobile in the early days of Earth's history when the intensity of internal heating by radioactive

Mesh	1	2	3	Variation	Variation
	400×50	800×100	1200×150	1 and 2	2 and 3
Time step	10^{-6}	5×10^{-7}	3.3×10^{-7}	—	—
Nu (averaged over $t=0.3$ to 0.5)	13.88	16.66	17.25	20%	3.5%

TABLE 1. Effect of mesh size and time step on the Nusselt number at the bottom of the flow domain for $Ra = 10^6$.

decay was much higher than today (Turcotte & Schubert 2002). The presently revealed variation of coupling modes with plate size, shown in figure 7(c), is under the assumption of pure bottom heating and no internal heating. An increase in internal heating increases plate mobility and therefore will probably lead to a decrease of the critical plate size of different modes. For example, the UMM appears only when the plate size is larger than approximately 2.5 for $Ra = 10^6$ with pure bottom heating. However, this value will probably decrease with the switching on of internal heating, and the appearance of the stagnant modes of SM I and SM II will probably be limited to smaller plates. Further simulations with internal heating switched on are worth pursuing to verify this.

Another simplification of the present study is the assumption of a uniform viscosity. In reality, the viscosity of the mantle is dependent on temperature, pressure and composition, which leads to a layering of viscosity with lower values in the upper mantle. The lowest viscosity value is present in the asthenosphere. This layering of mantle viscosity leads to long-wavelength flow, i.e. large convection cells with large horizontal extent (Bunge, Richards & Baumgardner 1996, 1997; Bunge & Richards 1996; Tackley 1996; Zhong *et al.* 2000; Lenardic, Richards & Busse 2006; Höink & Lenardic 2008). Consequently, the plate will move longer distances with the convective flow until it encounters impeding flow structures associated with downwellings, resulting in a decreased chance of being impeded. Further study of the coupling modes with a model that gives a closer representation of the Earth is worth pursuing in the future.

Acknowledgements

We thank A. van den Berg for helpful discussions. This work was supported by the National Natural Science Foundation of China (grant nos. 11472250 and 41630317 (Y.M.), 11472106 (J.Z.), 11572230 (J.-Q.Z.)).

Supplementary movies

Supplementary movies are available at <https://doi.org/10.1017/jfm.2019.189>.

Appendix. The mesh and time-step dependency test

The parameters of the mesh and time-step dependency test are listed in table 1. The time series of Nusselt number (Nu) at the bottom of the flow domain is shown in figure 17 for the three different meshes (400×50 , 800×100 , 1200×150) for the fixed-plate case with $L = 0.25$ and $Ra = 10^6$. The difference of Nu decreases from 20.0% between the former two meshes to 3.5% between the latter two. Based on

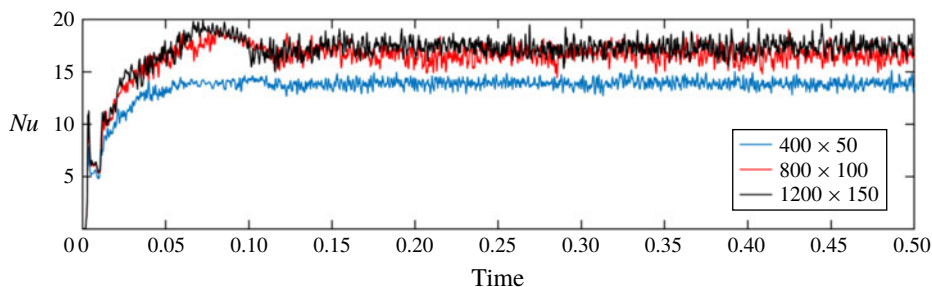


FIGURE 17. Time series of Nusselt number at the bottom of the flow domain for the fixed-plate case with $L=0.25$ and $Ra=10^6$.

this test, a mesh of 800×100 is adopted in the present simulations with a time step of 5×10^{-7} .

REFERENCES

- AHLERS, G., GROSSMANN, S. & LOHSE, D. 2009 Heat transfer and large scale dynamics in turbulent Rayleigh–Bénard convection. *Rev. Mod. Phys.* **81**, 503–537.
- BUNGE, H.-P. & RICHARDS, M. A. 1996 The origin of large scale structure in mantle convection: effects of plate motions and viscosity stratification. *Geophys. Res. Lett.* **23**, 2987–2990.
- BUNGE, H.-P., RICHARDS, M. A. & BAUMGARDNER, J.-R. 1996 Effect of depth-dependent viscosity on the planform of mantle convection. *Nature* **379**, 436–438.
- BUNGE, H.-P., RICHARDS, M. A. & BAUMGARDNER, J. R. 1997 A sensitivity study of three-dimensional spherical mantle convection at 10^8 Rayleigh number: effects of depth-dependent viscosity, heating mode, and an endothermic phase change. *J. Geophys. Res.* **102**, 11991–12007.
- BURKE, K. & TORSVIK, T. H. 2004 Derivation of large igneous provinces of the past 200 million years from long-term heterogeneities in the deep mantle. *Earth Planet. Sci. Lett.* **227**, 531–538.
- CANDE, S. C. & STOCK, J. M. 2004 Pacific–Antarctic–Australia motion and the formation of the Macquarie plate. *Geophys. J. Intl* **157**, 399–414.
- DAVIES, G. F. 1988 Role of the lithosphere in mantle convection. *J. Geophys. Res.* **93**, 10451–10466.
- EBINGER, C. J. & SLEEP, N. H. 1998 Cenozoic magmatism throughout east Africa resulting from impact of a single plume. *Nature* **395**, 788–791.
- ELDER, J. 1967 Convective self-propulsion of continents. *Nature* **214**, 657–750.
- GABLE, C. W., O’CONNELL, R. J. & TRAVIS, B. J. 1991 Convection in three dimensions with surface plates: generation of toroidal flow. *J. Geophys. Res.* **96**, 8391–8405.
- GRIGNÉ, C., LABROSSE, S. & TACKLEY, P. J. 2005 Convective heat transfer as a function of wavelength: implications for the cooling of the Earth. *J. Geophys. Res.* **110**, B03409.
- GRIGNÉ, C., LABROSSE, S. & TACKLEY, P. J. 2007 Convection under a lid of finite conductivity in wide aspect ratio models: effect of continents on the wavelength of mantle flow. *J. Geophys. Res.* **112**, B08403.
- GURNIS, M. 1988 Large-scale mantle convection and aggregation and dispersal of supercontinents. *Nature* **313**, 541–546.
- HERON, P. & LOWMAN, J. P. 2011 The effects of supercontinent size and thermal insulation on the formation of mantle plumes. *Tectonophysics* **510**, 28–38.
- HÖINK, T. & LENARDIC, A. 2008 Three-dimensional mantle convection simulations with a low-viscosity asthenosphere and the relationship between heat flow and the horizontal length scale of convection. *Geophys. Res. Lett.* **35**, L10304.
- HONDA, S., YOSHIDA, M., OOTORII, S. & IWASE, Y. 2000 The timescales of plume generation caused by continental aggregation. *Earth Planet. Sci. Lett.* **176**, 31–43.
- HOWARD, L. N., MALKUS, W. V. R. & WHITEHEAD, J. A. 1970 Self-convection of floating heat sources: a model for continental drift. *Geophys. Fluid Dyn.* **1**, 123–142.

- JARVIS, G. T. & PELTIER, W. R. 1989 Convection models and geophysical observations. In *Mantle Convection: Plate Tectonics and Global Dynamics* (ed. W. R. Peltier), pp. 479–594. Gordon and Breach.
- KING, S. D. 1995 The viscosity structure of the mantle. *Rev. Geophys.* **33**, 11–17.
- LENARDIC, A., MORESI, L., JELLINEK, A. M. & MANGA, M. 2005 Continental insulation, mantle cooling, and the surface area of oceans and continents. *Earth Planet. Sci. Lett.* **234**, 317–333.
- LENARDIC, A., RICHARDS, M. A. & BUSSE, F. H. 2006 Depth-dependent rheology and the horizontal length scale of mantle convection. *J. Geophys. Res.* **111**, B07404.
- LEONARD, B. P. 1979 A stable and accurate convective modelling procedure based on quadratic upstream interpolation. *Comput. Meth. Appl. Mech. Engng* **19**, 59–98.
- LITHGOW-BERTELLONI, C. & SILVER, P. G. 1998 Dynamic topography, plate driving forces and the African superswell. *Nature* **395**, 269–272.
- LOWMAN, J. P. & GABLE, C. W. 1999 Thermal evolution of the mantle following continental aggregation in 3D convection models. *Geophys. Res. Lett.* **26**, 2649–2652.
- LOWMAN, J. P. & JARVIS, G. T. 1993 Mantle convection flow reversals due to continental collisions. *Geophys. Res. Lett.* **20**, 2087–2090.
- LOWMAN, J. P. & JARVIS, G. T. 1995 Mantle convection models of continental collision and breakup incorporating finite thickness plates. *Phys. Earth Planet. Inter.* **88**, 53–68.
- LOWMAN, J. P. & JARVIS, G. T. 1999 Effects of mantle heat source distribution on supercontinent stability. *J. Geophys. Res.* **104**, B6, 12733–12746.
- LOWMAN, J., KING, S. D. & GABLE, C. W. 2001 The influence of tectonic plates on mantle convection patterns, temperature and heat flow. *Geophys. J. Intl* **146**, 619–636.
- MAO, Y., LEI, C. & PATTERSON, J. C. 2009 Unsteady natural convection in a triangular enclosure induced by absorption of radiation – a revisit by improved scaling analysis. *J. Fluid Mech.* **622**, 75–102.
- MAO, Y., LEI, C. & PATTERSON, J. C. 2010 Unsteady near-shore natural convection induced by surface cooling. *J. Fluid Mech.* **642**, 213–233.
- MITROVICA, J. X. 1996 Haskell [1935] revisited. *J. Geophys. Res.* **101**, 555–569.
- MONNEREAU, M. & QUÉRÉ, S. 2001 Spherical shell models of mantle convection with tectonic plates. *Earth Planet. Sci. Lett.* **184**, 575–587.
- PATANKAR, S. V. 1980 *Numerical Heat Transfer and Fluid Flow*. Taylor & Francis.
- PHILLIPS, B. R. & BUNGE, H.-P. 2005 Heterogeneity and time dependence in 3D spherical mantle convection models with continental drift. *Earth Planet. Sci. Lett.* **233**, 121–135.
- POLLACK, H. N., HURTER, S. J. & JOHNSON, J. R. 1993 Heat flow from the Earth's interior: analysis of the global data set. *Rev. Geophys.* **31**, 267–280.
- RITSEMA, J., VAN HEIJST, H. J. & WOODHOUSE, J. H. 1999 Complex shear wave velocity structure imaged beneath Africa and Iceland. *Science* **286**, 1925–1928.
- SCHUBERT, G., TURCOTTE, D. L. & OLSON, P. 2001 *Mantle Convection in the Earth and Planets*. Cambridge University Press, 940 pp.
- SUGGATE, R. P., STEVENS, G. R. & TE PUNGA, M. T. 1978 *The Geology of New Zealand*. Department of Scientific and Industrial Research.
- SUTHERLAND, R. 1999 Basement geology and tectonic development of the greater New Zealand region: an interpretation from regional magnetic data. *Tectonophysics* **308**, 341–362.
- TACKLEY, P. J. 1996 On the ability of phase transitions and viscosity layering to induce long wavelength heterogeneity in the mantle. *Geophys. Res. Lett.* **23**, 1985–1988.
- TORSVIK, T. H., BURKE, K., STEINBERGER, B., WEBB, S. J. & ASHWAL, L. D. 2010 Diamonds sampled by plumes from the core–mantle boundary. *Nature* **466**, 352–355.
- TORSVIK, T. H., STEINBERGER, B., COCKS, L. R. M. & BURKE, K. 2008 Longitude: linking Earth's ancient surface to its deep interior. *Earth Planet. Sci. Lett.* **276**, 273–282.
- TURCOTTE, D. & SCHUBERT, G. 2002 *Geodynamics*, 2nd edn. Cambridge University Press.
- WHITEHEAD, J. A. 1972 Moving heaters as a model of continental drift. *Phys. Earth Planet. Inter.* **5**, 199–212.
- WHITEHEAD, J. A. & BEHN, M. D. 2015 The continental drift convection cell. *Geophys. Res. Lett.* **42**, 4301–4308.

- WHITEHEAD, J. A., SHEA, E. & BEHN, M. D. 2011 Cellular convection in a chamber with a warm surface raft. *Phys. Fluids* **23**, 104103.
- ZHANG, J. & LIBCHABER, A. 2000 Periodic boundary motion in thermal turbulence. *Phys. Rev. Lett.* **84**, 4361–4364.
- ZHONG, J.-Q. & ZHANG, J. 2005 Thermal convection with a freely moving top boundary. *Phys. Fluids* **17**, 115105.
- ZHONG, J.-Q. & ZHANG, J. 2007a Dynamical states of a mobile heat blanket on a thermally convecting fluid. *Phys. Rev. E* **75**, 055301.
- ZHONG, J.-Q. & ZHANG, J. 2007b Modeling the dynamics of a free boundary on turbulent thermal convection. *Phys. Rev. E* **76**, 016307.
- ZHONG, S. & GURNIS, M. 1993 Dynamic feedback between a Continent like raft and thermal convection. *J. Geophys. Res.* **98**, 12219–12232.
- ZHONG, S., ZUBER, M. T., MORESI, L. & GURNIS, M. 2000 Role of temperature-dependent viscosity and surface plates in spherical shell models of mantle convection. *J. Geophys. Res.* **105**, 11063–11082.